npj | quantum materials

www.nature.com/npjquantmats

REVIEW ARTICLE OPEN

# Unconventional charge order and superconductivity in kagome-lattice systems as seen by muon-spin rotation

Z. Guguchia[1]✉, R. Khasanov[1] and H. Luetkens[1]

Kagome lattices are intriguing and rich platforms for studying the intertwining of topology, electron correlation, and magnetism. These materials have been subject to tremendous experimental and theoretical studies not only due to their exciting physical properties but also as systems that may solve critical technological problems. We will review recent experimental progress on superconductivity and magnetic fingerprints of charge order in several kagome-lattice systems from the local-magnetic probe point of view by utilizing muon-spin rotation under extreme conditions, i.e., hydrostatic pressure, ultra low temperature and high magnetic field. The systems include: (1) The series of compounds $AV_3Sb_5$ ($A$ = K, Rb, Cs) with V kagome lattice which form the first kagome-based family that exhibits a cascade of symmetry-broken electronic orders, including charge order and superconductivity. In these systems, we find a time-reversal symmetry-breaking charge ordered state and tunable unconventional time-reversal symmetry-breaking superconductivity. (2) The system $LaRu_3Si_2$ with distorted kagome layers of Ru, in which our experiments and calculations taken together point to nodeless moderate coupling superconductivity. It was also found that the electron-phonon coupling alone can only explain a small fraction of $T_c$ from calculations, which suggests other factors enhancing $T_c$ such as the correlation effect from the kagome flat band, the van Hove point on the kagome lattice, and the high density of states from the narrow kagome bands. (3) $CeRu_2$ with a pristine Ru kagome lattice, which we classify as an exceedingly rare nodeless (with anisotropic $s$-wave gap symmetry) magnetic kagome superconductor.

*npj Quantum Materials* (2023)8:41 ; https://doi.org/10.1038/s41535-023-00574-7

## INTRODUCTION

Layered systems, with highly anisotropic electronic properties have been found to be potential hosts for rich, unconventional and exotic quantum states and are a valuable resources for building quantum matter by design. In quantum materials, in which significant number of electrons are moving in complicated periodic system of many atoms, several degrees of freedom and interactions needs to be considered: spin, charge and lattice. One of the central threads of quantum materials research is correlated electron physics[1,2] in which strong electron-electron interactions lead to new phenomena such as Mott insulator, superconductivity, quantum criticality and etc. In simple metals it is rather easy for the electron-phonon interaction to overcome the Coulomb repulsion through the retardation effect. In so-called strongly correlated electron systems, Coulomb interaction dominates over the attractive electron-phonon coupling. Another important interaction is the spin-orbit coupling, which is recognized as an essential ingredient in forming certain topological phases with non-trivial band topology[3–5]: e.g., topological insulators. Non-trivial topology can also appear in gapless phases, such as in the Weyl semimetals[6–8], where low energy quasi particle excitations are Weyl fermions. Weyl cones act as sources and sinks of Berry curvature, being essential for topological phases. In some materials, these two threads come together and lead to new correlated topological quantum states. Such topological state can be manipulated by tuning correlation effects. Manipulation of topological states is essential for fundamental physics and next-generation quantum technology.

Several layered systems with kagome lattices[9–14], two-dimensional lattices of corner-sharing triangles, have been demonstrated to be intriguing and rich platforms for studying the intertwining of topology, correlation, and magnetism. The kagome pattern originates from Japanese basketry (see Fig. 1a, kago - Bamboo basket, me - woven pattern). Tremendous efforts have been made to study magnetic degrees of freedom, since by decorating kagome lattice with magnetic moments one can realize non-collinear antiferromagentic states[15,16], quantum spin-liquid states[17–19] or ferromagnetic Weyl-semimetallic states[11,20,21] with large intrinsic anomalous Hall effect. Kagome lattices have also long been an interest in terms of band structure. Single orbital tight-binding model gives a band structure which shows a coexistence of a couple of interesting features: topological physics associated with Dirac points in the spectrum, and electron-electron correlation physics realized through a flat band and inflection points which lead to van Hove singularities in the DOS (see Fig. 1b). Flat band and van Hove singularities drastically enhance the DOS (see Fig. 1c), thereby promoting electron correlation effects[22]. More broadly, there is a long history of predicting[23,24] different types of electronic instabilities on the kagome lattices at select fillings (e.g., 5/4 electrons per band) such as charge-density wave order, bond density wave state, chiral spin density wave state, and unconventional superconductivity with $d+id$- or $f$-wave superconductivity. Unconventional superconductivity refers to superconductors where the Cooper pairs are not bound together by phonon exchange but instead by exchange of some other kind, in particular, based on effective interaction originating from spin fluctuations. Unconventional superconductivity is characterized by condensates of Cooper pairs of lower symmetry, in contrast to the conventional superconductors with the most symmetric Cooper pairs. Alternative pairing mechanism and strong correlation effects are key elements to prevent electrons from undergoing conventional $s$-wave pairing.

[1]Laboratory for Muon Spin Spectroscopy, Paul Scherrer Institute, CH-5232 Villigen PSI, Switzerland. ✉email: zurab.guguchia@psi.ch

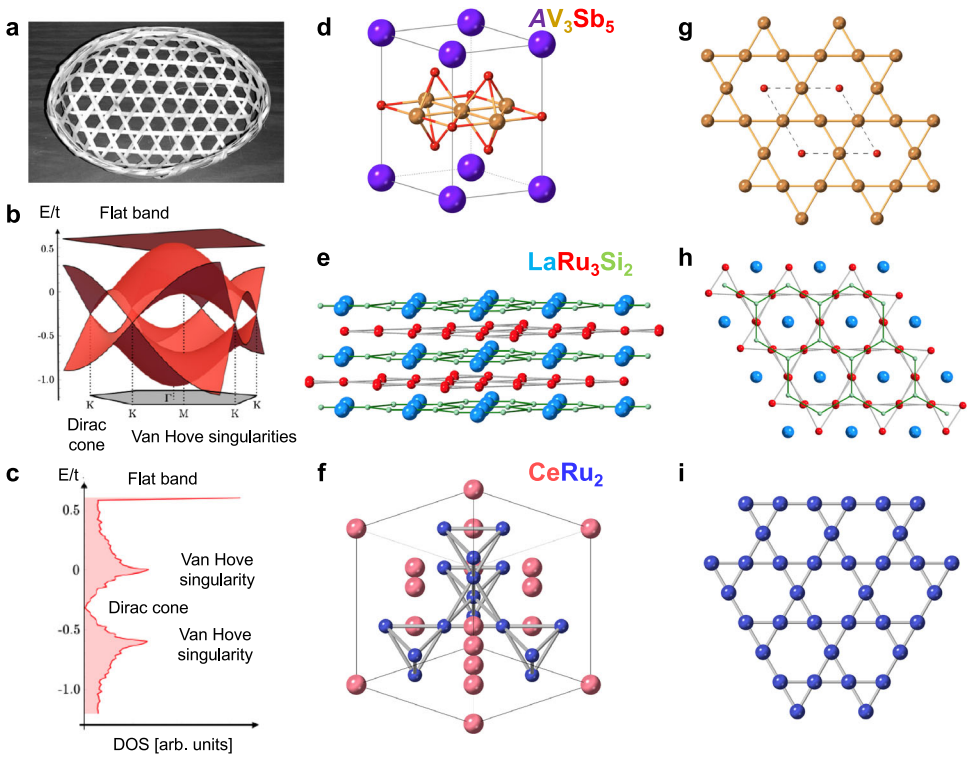


**Fig. 1 Kagome systems and their electronic and crystal structure. a** The kagome pattern originates from Japanese basketry. **b** The electronic structure contains van Hove singularities, Dirac cones, and a flat band. **c** The flat band and the van Hove singularities drastically enhance the density of states (DOS), thereby promoting interactions (after ref. [22]). Three dimensional representation (**d**, **e**, **f**) and top view (**g**, **h**, **i**) of the atomic structure of $AV_3Sb_5$, $LaRu_3Si_2$, and $CeRu_2$, respectively (adapted from refs. [66,76,82]).

Regarding the charge density wave (CDW), it is a static modulation of conduction electrons and is a Fermi-surface driven phenomenon usually accompanied by a periodic distortion of the lattice. In essence, the electronic energy of the solid is lowered as a consequence of the lattice distortion, the attendant strain energy of which is more than compensated by the reduction in electronic energy. The present understanding of CDWs in conductors follows from the pioneering work of Peierls[25], Kohn[26] and Overhauser[27]. A favorable Fermi surface geometry is necessary for the formation of a CDW, which will most likely occur when the shape of the Fermi surface permits a connection by the same wavevector Q, i.e., $Q = 2k_f$. This modulation with wavevector Q will modify the Fermi surface by creating gaps at these nested positions. If the nested (i.e., dimpled) portion of the Fermi surface is significant, the energy gain by creating energy gaps may overcome the energy cost arising from the strain associated with the periodic lattice distortion, thus allowing the formation of a CDW. Another requirement for forming a CDW is a strong electron-phonon coupling, required to permit ionic displacements to reduce the otherwise prohibitive Coulomb energy, and precursor phenomena such as a soft phonon mode (Chan and Heine[28]) might occur above the transition temperature to assist the CDW instability. Numerous examples of a CDW phase change have recently been found in quasi-one-dimensional organic conductors[29], quasi-two-dimensional layered compounds (e.g., transition-metal dichalcogenides[30], cuprate high-temperaure superconductors[31,32]). In lower-dimensional systems (1–d and 2–d materials) the possibility of CDW formation is enhanced because the simple structures involved lead to a high probability for favorable Fermi surface nesting. But in three-dimensional materials CDW phenomena should, in principle, be rather rare because of the unlikelihood of favorable Fermi surface nesting.

Materials realizing the interplay between superconductivity, charge order and electronic band topology has long be awaited. The recently discovered family of kagome metals $AV_3Sb_5$ ($A$ = K, Rb, Cs)[33–37] exhibit an array of interesting effects such as giant anomalous Hall conductivity[38,39], charge order[40–46], orbital order[47], switchable chiral transport[48] and superconductivity[33–37]. $AV_3Sb_5$ ($A$ = K, Rb, Cs) exhibit a layered structure of V-Sb sheets intercalated by K,Rb,Cs (see Fig. 1d). The vanadium sublattice is a structurally perfect kagome lattice (see Fig. 1g). There are two distinct Sb sublattices. The sublattice formed by Sb1 atoms is a simple hexagonal net, centerd on each kagome hexagon. The Sb2 sublattice creates a graphen like Sb sheet below and above each kagome layer. The Fermi level in these compounds is in close proximity to several Dirac points and saddle points. Theoretically, the normal state band structure features $Z_2$ topological invariants, which have topologically protected surface states[33,34,49]. There are various theoretical works determining the leading and subleading instabilities in these kagome metals[50–57]. Various mechanisms to induce charge order in kagome metals have been suggested[50–57]. More importantly, there are proposals of couple of different orbital currents and chiral flux phases, which implies that the charge-ordered state displays not only bond distortions, but also orbital current loops[50–58] around both the honeycomb and triangular plaquettes. High-temperature time-reversal symmetry-breaking (TRSB) charge order is extremely rare, and finds a direct comparison with the fundamental Haldane[59] model for the honeycomb lattice and Varma[60,61] model for the square lattice. Such exotic charge order[40–42] in the kagome superconductor $AV_3Sb_5$ ($A$ = K, Rb, Cs) has been originally suggested by scanning tunneling microscopy, that observes a chiral $2 \times 2$ charge order with an unusual magnetic field response[40–42]. Theoretical analysis[50,62–65] also suggests that this chiral charge order can not only lead to a giant anomalous Hall effect[38] but also be a precursor of unconventional superconductivity[64]. In sum, $AV_3Sb_5$ is the first material class of kagome-lattice systems which was proposed to exhibit chiral charge order, combined with

superconductivity and topological transport, producing an intriguing combination of physical phenomena. However, direct evidence for time-reversal symmetry-breaking charge order (which would provide the smoking gun evidence for the existence of orbital currents) was missing. Using muon-spin rotation technique we provided systematic evidence for the existence of time-reversal symmetry-breaking by charge order and for the unconventional nature of superconductivity[22,66–70].

The layered system $LaRu_3Si_2$[71–75] is another good example of a material hosting both a kagome lattice and superconductivity. The structure of $LaRu_3Si_2$ contains distorted kagome layers of Ru sandwiched between layers of La and layers of Si having a honeycomb structure (see Fig. 1e and h), crystallizing in the $P6_3/m$ space group. The system was shown to be a typical type II superconductor with a superconducting (SC) transition temperature with an onset as high as $\simeq 7$ K[73]. It has the highest SC transition temperature among the kagome-lattice materials. Anomalous properties[75] in the normal and SC states[73] were reported in $LaRu_3Si_2$, such as the deviation of the normal state specific heat from the Debye model, non-mean field like suppression of superconductivity with magnetic field and non-linear field dependence of the induced quasiparticle density of states (DOS). However, for the most part only the critical temperatures and fields had been determined for the superconducting state of $LaRu_3Si_2$ and the connection to kagome lattice physics had been missing. Thus, we carried out thorough and microscopic exploration of superconductivity in $LaRu_3Si_2$[76] from both experimental and theoretical perspectives in order to understand the origin of the relatively high value of the critical temperature.

Yet another superconductor with a kagome lattice is $CeRu_2$ that was discovered over 60 years ago[77] but the relevance of kagome lattice physics has long been overlooked. The distorted Laves-phase superconductor $CeRu_2$ takes a cubic structure (Fig. 1f)[78] with two different Ce sites and it reveals a pristine Ru kagome lattice in the plane perpendicular to the [111] direction (Fig. 1i) that contributes to the electronic properties. Indeed, the normal state band structure features a kagome flat band, Dirac points and van Hove singularities formed by the Ru-$dz^2$ orbitals near the Fermi level[79], which are predicted to support topologically nontrivial states[79]. Much attention has been paid to the unusual superconducting state in $CeRu_2$, which shows two separate regions of magnetic hysteresis[80,81].

In this review article, we will review recent experimental progress on unconventional aspects of superconductivity/magnetism and on magnetic fingerprints of charge order in several kagome-lattice systems $AV_3Sb_5$[22,66–70], $LaRu_3Si_2$[76], and $CeRu_2$[82] by combining zero-field, high-field, high-pressure and ultra low temperature muon-spin rotation techniques.

## μSR TECHNIQUE: A VERY SENSITIVE MICROSCOPIC PROBE

The acronym μSR stands for muon spin rotation, or relaxation, or resonance, depending respectively on whether the muon spin motion is predominantly a rotation, or a relaxation towards an equilibrium direction, or a more complex dynamics dictated by the addition of short radio frequency pulses. This technique allows us to study fundamental problems related to superconductivity[83,84] and also serve as an extremely sensitive local probe to detect small internal magnetic fields and ordered magnetic volume fractions in the bulk of magnetic materials[85–89]. Moreover, μSR is also valuable for studying materials in which magnetic order is random or of short range. This makes μSR a perfectly complementary technique to scattering techniques such as neutron diffraction, which is used to determine crystallographic and magnetic structures. Moreover, the μSR technique has a unique time window ($10^{-4}$ s to $10^{-11}$ s) for the study of magnetic fluctuations in materials, which is complementary to other

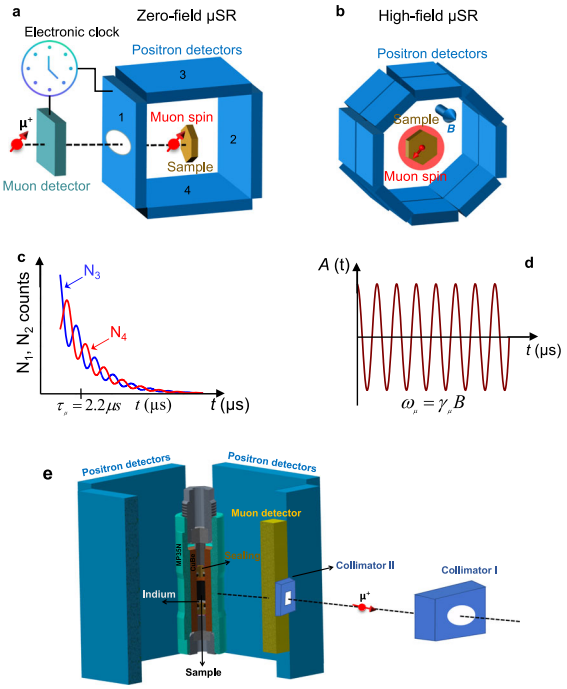


**Fig. 2 Overview of the experimental setups and pressure cell for μSR. a** A schematic overview of the ZF-μSR experimental setup. Spin polarized muons with spin $S_\mu$, forming 60° with the momentum of the muon, are implanted in the sample. The sample was surrounded by four detectors: Forward (1), Backward (2), Up (3), and Down (4). An electronic clock is started at the time the muon passes the muon detector and is stopped as soon as the decay positron is detected in the positron detectors. **b** Schematic overview of the high field μSR experimental setup for the muon spin forming 90° with respect to the momentum of the muon. The sample was surrounded by 2 times 8 positron detectors, arranged in rings. The specimen was mounted in a He gas-flow cryostat with the largest face perpendicular to the muon beam direction, along which the external field was applied. Behind the sample lies a veto counter (in orange) which rejects the muons that do not hit the sample. **c** The number of detected positrons $N_3$ and $N_4$ as a function of time for the up and down detector, respectively. The magnetic field is applied in the beam direction. **d** The so-called asymmetry (or μSR) signal is obtained by essentially building the difference between $N_3$ and $N_4$. **e** Fully assembled typical double-wall piston-cylinder type of pressure cell used in our μSR experiments. The schematic view of the positron and muon detectors at the GPD spectrometer are also shown. In reality, each positron detector consists of three segments. The collimators reduce the size of the incoming muon beam. Figures are adapted from refs. [66,67].

experimental techniques such as neutron scattering, NMR, or magnetic susceptibility. With its unique capabilities, μSR should be considered to play an important role in determining unconventional aspects of superconductivity and magnetic fingerprints of charge order in the kagome-lattice systems, which are interesting due to both fundamental and practical aspects. A brief introduction to the μSR technique[83,89–91] is given below.

The μSR method is based on the observation of the time evolution of the spin polarization $\vec{P}(t)$ of the muon ensemble. A schematic overview of the zero-field μSR experimental setup with the muon spin forming 60° with respect to the muon momentum is shown in Fig. 2a. In a μSR experiments an intense beam (momentum $p_\mu = 29$ MeV/c) of 100% spin-polarized muons is stopped in the sample. The positively charged muons $\mu^+$ thermalize in the sample at interstitial lattice sites, where they act as magnetic microprobes. In a magnetic material the muon spins precess in the local field $B_\mu$ at the muon site with the Larmor frequency $2\pi\nu_\mu = \gamma_\mu B_\mu$ (muon gyromagnetic ratio $\gamma_\mu/(2\pi) = 135.5$ MHz T$^{-1}$).

The muons implanted into the sample will decay after a mean life time of $\tau_\mu = 2.2$ μs, emitting a fast positron $e^+$ preferentially along their spin direction. Various detectors placed around the sample track the incoming $\mu^+$ and the outgoing $e^+$ (see Fig. 2a). Namely, the sample is surrounded by four positron detectors: Forward (1), Backward (2), Up (3), and Down (4). When the muon detector records the arrival of a μ in the specimen, the electronic clock starts. The clock is stopped when the decay positron $e^+$ is registered in one of the $e^+$ detectors, and the measured time interval is stored in a histogramming memory. In this way a positron-count versus time histogram is formed (Fig. 2c). A muon decay event requires that within a certain time interval after a $\mu^+$ has stopped in the sample only one $e^+$ and no other particle is detected. This time interval extends usually over several muon lifetimes (e.g., 10 μs). After a number of muons has stopped in the sample, one obtains a histogram for the forward ($N_1^{e^+}$) and the backward ($N_2^{e^+}$) detectors as shown in Fig. 2c, which in the ideal case has the following form:

$$N_\alpha^{e^+}(t) = N_0 e^{-\frac{t}{\tau_\mu}}(1 + A_0 \overrightarrow{P}(t)\hat{n}_\alpha) + N_{bgr}. \alpha = 1, 2 \quad (1)$$

Here, the exponential factor accounts for the radioactive muon decay. $\overrightarrow{P}(t)$ is the muon-spin polarization function with the unit vector $\hat{n}_\alpha$ ($\alpha = 1,2$) with respect to the incoming muon spin polarization. $N_0$ is a parameter that scales with the accumulated number of positron events in the spectra. $N_{\rm bgr}$ is a background contribution due to uncorrelated starts and stops. $A_0$ is the initial asymmetry, depending on different experimental factors, such as the detector solid angle, efficiency, absorption, and scattering of positrons in the material. Typical values of $A_0$ are between 0.2 and 0.3.

Since the positrons are emitted predominantly in the direction of the muon spin which precesses with $\omega_\mu = 2\pi\nu_\mu$, the Forward and Backward detectors will detect a signal oscillating with the same frequency. In order to remove the exponential decay due to the finite life time of the muon, the so-called asymmetry signal $A(t)$ is calculated (see Fig. 2d) (after subtracting the background $N_{bgr}$ from each $N(t)$):

$$A(t) = \frac{N_1^{e^+}(t) - N_2^{e^+}(t)}{N_1^{e^+}(t) + N_2^{e^+}(t)} = A_0 P(t), \quad (2)$$

where $N_1^{e^+}(t)$ and $N_2^{e^+}(t)$ are the number of positrons detected in the forward and backward detectors, respectively. The quantities $A(t)$ and $P(t)$ depend sensitively on the spatial distribution and dynamical fluctuations of the magnetic environment of the muons. Hence, these functions allow us to study interesting physics of the investigated system.

To cope with the increasing demand of the users, the laboratory for muon spin spectroscopy at the Paul Scherrer Institue is permanently enhancing the level of its μSR Facilities. Much effort has been put recently on technical aspects like the improvement of the signal/background ratio, improved electronics, automatization and user-friendliness. The sample environment has also been widely extended. The available field range was extended up to 9.5 T in line with improved time resolution[92] at the high-field HAL-9500 instruments at the Swiss Muon Source (S$\mu$S), which opened the window for the observation of precession frequencies of 1.4 GHz and of correlation times of field fluctuations of less than 3 ns[92]. A schematic overview of the experimental setup for the high-field μSR instrument is shown in the inset of Fig. 2b. The muon spin forms 90° with respect to the muon momentum. The sample is surrounded by $2 \times 8$ positron detectors, arranged in rings. HAL-9500 is equipped with He gas-flow cryostat and BlueFors vacuum-loaded cryogen-free dilution refrigerator, allowing to cover the temperature range between 12 mK and 300 K.

High-pressure cells suitable for μSR experiments have also been developed, so that external hydrostatic pressures up to 2.5 GPa can be applied to the samples and measurements down to mK temperatures can be performed[93–97]. μSR experiments under pressure are performed at the $\mu$E1 beamline of the Paul Scherrer Institute (Villigen, Switzerland) using the instrument GPD, where an intense high-energy ($p_\mu = 100$ MeV/c) beam of muons is implanted in the sample through the pressure cell walls. The GPD instrument is equipped with $^3$He insets (base temperature $\simeq 0.25$ K) for a $^4$He cryostat. Pressures up to 1.9 GPa and 2.3 GPa are generated in a double wall piston-cylinder type cell made of CuBe/MP35N and MP35N/MP35N, respectively, specially designed to perform μSR experiments under pressure[93,95]. A fully assembled typical double-wall pressure cell is presented in Fig. 1e. The body of the pressure cell consists of two parts: the inner and the outer cylinders which are shrink-fitted into each other. The outer body of the cell is made out of MP35N alloy. The inner body of the cell is made out of CuBe alloy. Other components of the cell are: pistons, mushroom shaped part, seals, locking nuts, and spacers. The mushroom pieces and sealing rings are made out of non hardened CuBe. With both pistons completely inserted, the maximum sample height is 12 mm. As a pressure transmitting medium Daphne oil 7373 is used. The pressure is measured by tracking the superconducting transition of a very small indium plate by AC susceptibility[93]. The filling factor of the pressure cell is maximized in order to obtain a fraction of the muons stopping in the sample of ~40–50%.

## KAGOME MATERIALS $AV_3SB_5$ ($A = K, RB, CS$)

### Time-reversal symmetry breaking charge order

Discovering exotic intertwined charge order is at the frontier of quantum physics. Orbital-current-induced time-reversal symmetry-breaking charge order has long been expected to generate a quantum anomalous Hall effect[59] (the subject of Haldane's Nobel prize-winning work) and constitute the hidden matter phase in high-temperature superconductivity (from the well-known Varma model[60]). Experimental realization of this phenomenon is exceptionally challenging, as materials exhibiting orbital currents are rare and the characteristic signals of orbital currents are often too weak to be detected. Such exotic charge order had been discussed in the kagome superconductor family $AV_3Sb_5$ using charge sensitive probes and theoretical analysis[40–42,50,62–65]. However, direct magnetic probe evidence for time-reversal symmetry-breaking charge order had been missing. Muon spin rotation/relaxation (μSR) has long been regarded as the most sensitive probe for any time-reversal symmetry-breaking signal. We used the PSI μSR facility to provide[66–68] systematic evidence for the existence of time-reversal symmetry-breaking by charge order by combining zero-field and high-field μSR techniques.

The ZF-μSR spectra in all three systems $AV_3Sb_5$ ($A$ = K, Rb, Cs) are characterized by a weak depolarization of the muon spin ensemble and show no evidence of long-range ordered magnetism (see Fig. 3a, where a ZF-μSR spectrum for $KV_3Sb_5$ is shown). However, the measurements show that the muon spin relaxation has a clearly observable temperature dependence. The zero-field relaxation is decoupled by the application of a small external magnetic field applied longitudinal to the muon spin polarization, $B_{\rm LF} = 50$ G[66–68,98]. Therefore the observed relaxation is due to spontaneous fields which are static on the microsecond timescale. The zero-field μSR spectra for single crystalline as well as for polycrystalline samples of $AV_3Sb_5$ ($A$ = K, Rb, Cs)[66–68,99] were fitted using the gaussian Kubo-Toyabe depolarization function[100], which reflects the field distribution at the muon site created by the nuclear moments of the sample, multiplied by an additional exponential exp(-$\Gamma t$) term (see Fig. 3a):

$$P_{ZF}^{GKT}(t) = \left(\frac{1}{3} + \frac{2}{3}\left(1 - \Delta^2 t^2\right)\exp\left[-\frac{\Delta^2 t^2}{2}\right]\right)\exp(-\Gamma t) \quad (3)$$

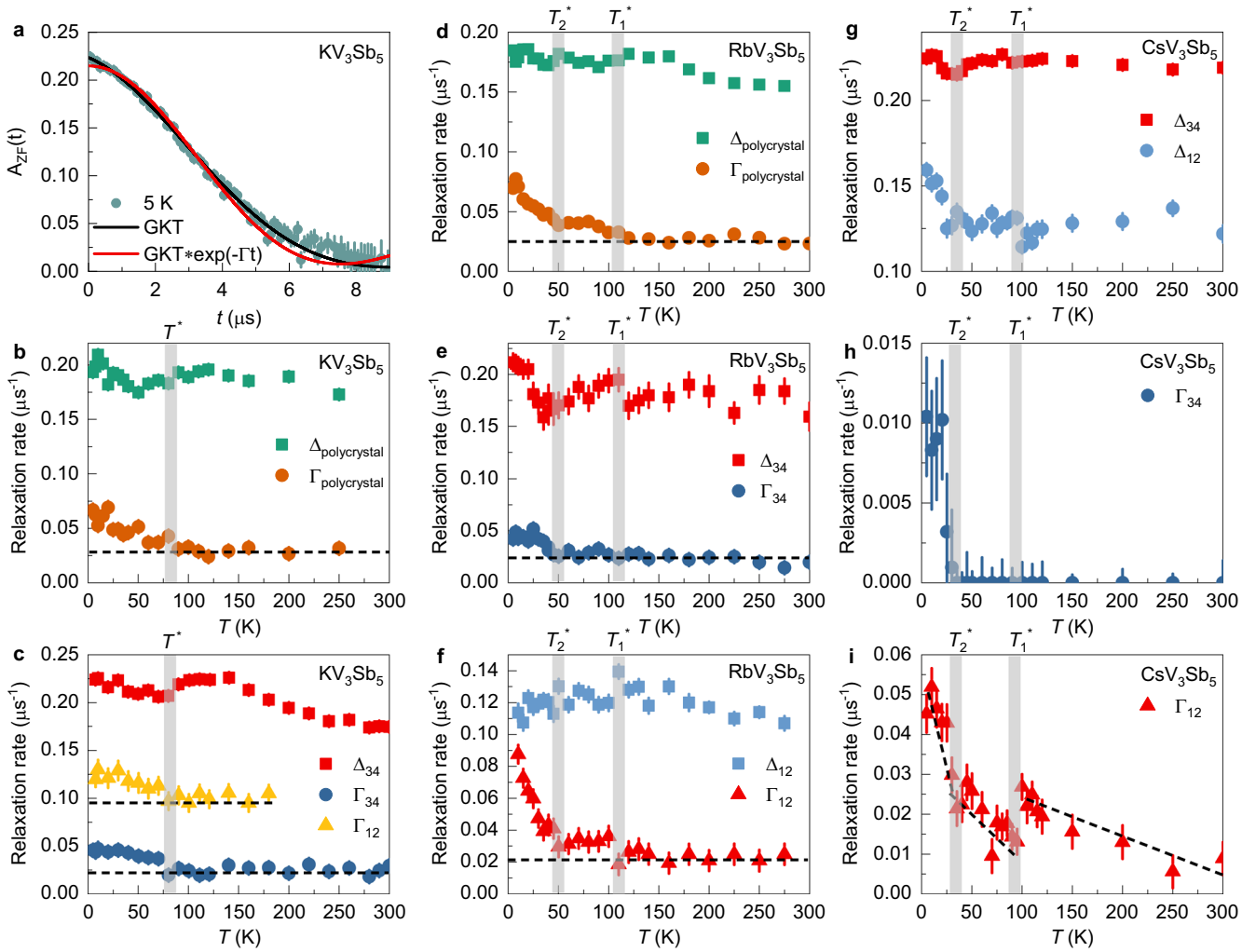


**Fig. 3 Indication of time-reversal symmetry-breaking of the charge order in $KV_3Sb_5$, $RbV_3Sb_5$ and $CsV_3Sb_5$. a** The ZF μSR time spectra for $KV_3Sb_5$, obtained at $T = 5$K from detectors 3 and 4. The solid curves represent fits to the recorded time spectra, using only Gaussian Kubo Toyabe (GKT) function (black) and the one where an additional exponential exp(-Γ*t*) term (red) is multiplied to the GKT function. Error bars are the standard error of the mean (s.e.m.) for about $10^6$ events. **b** The temperature dependences of the relaxation rates $\Delta_{polycrystal}$ and $\Gamma_{polycrystal}$ for the polycrystalline sample of $KV_3Sb_5$, obtained in a wide temperature range. **c** The temperature dependence of Γ and Δ from two sets of detectors. The vertical gray lines mark the concomitant time-reversal symmetry-breaking and charge ordering temperature $T^* \simeq 80$ K. The temperature dependences of the relaxation rates Γ and Δ for the polycrystalline (**d**) and single crystalline (**e**, **f**) samples of $RbV_3Sb_5$. **e**, **f** These show the results from detectors 3 and 4 and 1 and 2, respectively. The temperature dependences of the nuclear relaxation rates $\Delta_{34}$ and $\Delta_{12}$ (**g**), as well as the electronic relaxation rates $\Gamma_{34}$ (**h**) and $\Gamma_{12}$ (**i**) for the single crystal of $CsV_3Sb_5$. The error bars represent the standard deviation of the fit parameters. The data are taken from refs. [66–68].

where $\Delta/\gamma_\mu$ is the width of the local field distribution due to the nuclear moments. However, this Gaussian component may also include the field distribution at the muon site created by a dense network of weak electronic moments. $\gamma_\mu/2\pi = 135.5$ MHz/T is the muon gyromagnetic ratio. A gaussian Kubo Toyabe (GKT) shape is expected due to the presence of the dense system of nuclear moments with large values of nuclear spins ($I = 3/2$ for $^{39}$K, $I = 7/2$ for $^{51}$V, and $I = 5/2$ for $^{121}$Sb) in $AV_3Sb_5$ and a high natural abundance. The observed deviation from a pure GKT behavior in paramagnetic systems is frequently observed in μSR measurements. This can e.g., be due to a mixture of diluted and dense nuclear moments, the presence of electric field gradients or a contribution of electronic origin. The relaxation in single crystals might also be not GKT-like due to the fact that the quantization axis for the nuclear moments depends on the electric field gradients[101]. Naturally this is also often responsible for an anisotropy of the nuclear relaxation. As this effect essentially averages out in polycrystalline samples, we would like to mention that we also observed the additional exponential term in the polycrystalline sample of $KV_3Sb_5$, which indicates that this effect is probably not the dominant in our single crystal measurements. Our high field μSR results presented below however prove that there is indeed a strong contribution of electronic origin to the muon spin relaxation below the charge ordering temperature. Therefore, we conclude that Γ in zero magnetic field also tracks the temperature dependence of the electronic contribution, as we discussed previously[66–68]. But we cannot exclude subtle effects due to changes in the electric field gradients in the charge ordered state[66]. Figure 3b shows the temperature dependence of the Gaussian and exponential relaxation rates Δ and Γ, respectively, for the polycrystalline sample of $KV_3Sb_5$. There is a clear increase immediately visible in the exponential relaxation rate upon lowering the temperature below the charge ordering temperature $T^* \simeq 75$ K. This observation indicates the enhanced spread of internal fields sensed by the muon ensemble concurrent with the onset of charge ordering. The enhanced magnetic response that sets in with the charge order persists all the way down to the base

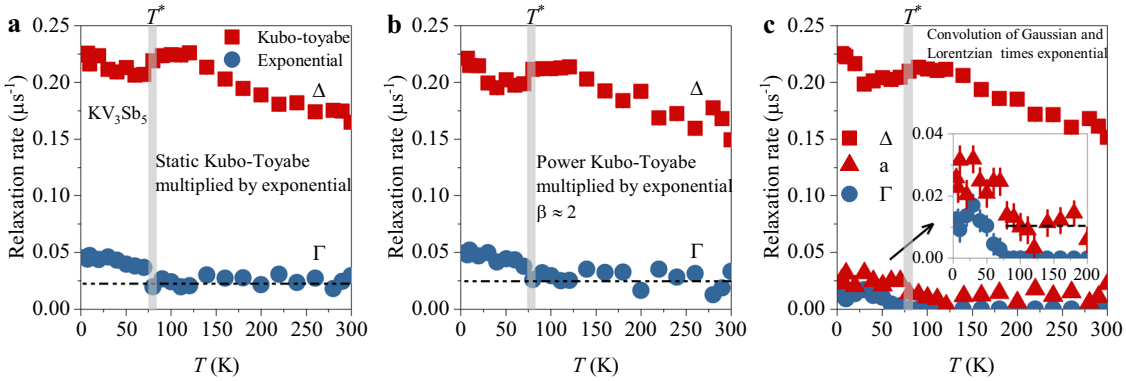


**Fig. 4 The results of zero-field μSR data analysis using various models for $KV_3Sb_5$. a** The ZF μSR time spectra for $KV_3Sb_5$, obtained at $T = 5$ K from detectors 3 and 4. The solid curves represent fits to the recorded time spectra, using Eq. 4 and Eq. 5 (the latter multiplied by an additional exponential exp(-Γ$t$) term. Error bars are the standard error of the mean (s.e.m.) for about $10^6$ events. **b** Power Kubo-Toyabe function multiplied by an additional exponential. **c** Function with the convolution of the Gaussian and Lorentzian distributions multiplied by an additional exponential.

temperature, and remains constant across the superconducting transition[66]. Increase of the internal field width visible from the ZF-μSR relaxation rate corresponds to an anomaly seen also in the nuclear contribution to the relaxation rate Δ; namely, a peak coinciding with the onset of the charge order, which decreases to a broad minimum before increasing again towards lower temperatures. The temperature dependence of both the muon spin relaxation rates $\Delta_{12,34}$ and $\Gamma_{12,34}$ (from two different sets of detectors) over a broad temperature range from the base temperature to 300 K for the single crystalline sample of $KV_3Sb_5$ is shown in Fig. 3c. The enhanced electronic relaxation rate below $T^* \simeq 75$ K is seen in both $\Gamma_{12}$ and $\Gamma_{34}$. This indicates that the internal field at the muon site has an out-of-plane component as well as an in-plane component. The increase in the exponential relaxation below $T^*$ is estimated to be $\simeq 0.025\ \mu s^{-1}$, which can be interpreted as a characteristic field strength $\Gamma_{12}/\gamma_\mu \simeq 0.3$ G. We note that a similar value of internal magnetic field strength is reported in several time-reversal symmetry-breaking superconductors[102–105].

Zero-field μSR results for the polycrystalline and single crystal samples of $RbV_3Sb_5$[67] are shown in Fig. 3d–f. Namely, the temperature dependence of the Gaussian and exponential relaxation rates Δ and Γ, respectively, for the polycrystalline sample of $RbV_3Sb_5$ are shown. The main observation is the two-step increase of the relaxation rate Γ, consisting of a noticeable enhancement at $T_1^* \simeq 110$ K, which corresponds to the charge-order transition temperature $T_{co}$, and a stronger increase below $T_2^* \simeq 50$ K. To substantiate this result, data from the single crystals are presented in Fig. 3e, f. The data from the up-down (34) and forward-backward (12) sets of detectors not only confirm the increase of Γ, but also shed more light into the origin of the two-step behavior. In particular, while $\Gamma_{34}$ (see Fig. 3e) is enhanced mostly below $T_2^* \simeq 50$ K, $\Gamma_{12}$ (see Fig. 3f) also features a mild initial increase right below $T_1^* \simeq 110$ K. Since the enhanced electronic relaxation rate below $T_1^*$ is seen mostly in $\Gamma_{12}$, it indicates that the local field at the muon site lies mostly within the *ab*-plane of the crystal. Below $T_2^*$, the internal field also acquires an out-of-plane component, as manifested by the enhancement of both $\Gamma_{12}$ and $\Gamma_{34}$. The increase of the electronic contribution to the internal field width is also accompanied by maxima and minima in the temperature dependence of the nuclear contribution to the internal field width $\Delta/\gamma_\mu$, particularly for the up-down set of detectors (see Fig. 3e). The increase in the exponential relaxation of $RbV_3Sb_5$ between $T_1^*$ and 2 K is about 0.05 $\mu s^{-1}$, which corresponds to a characteristic field strength $\Gamma_{12}/\gamma_\mu \simeq 0.6$ G.

Zero-field μSR results for the single crystal sample of $CsV_3Sb_5$[68] are shown in Fig. 3g–i. Upon lowering the temperature below $T_1^* = T_{CDW}$, $\Gamma_{12}$ increase with two different slopes above and below the characteristic temperature $T_2^* \simeq 30$ K (see Fig. 3i). $\Gamma_{34}$ remains zero down to $T_2^*$ below which it shows an increase (see Fig. 3h). This indicates that the local fields at the muon stopping site were found to be confined within the crystallographic *ab* plane for temperatures between $T_1^* \simeq 90$ K and $T_2^* \simeq 30$ K, while they possesses a pronounced out-of-plane component below $T_2^*$. The increase of the exponential contribution to the internal field width is also accompanied by a non-monotonic temperature dependence of the Gaussian contribution to the internal field width (see Fig. 3g). The appearance of a step-like change of both Δ and Γ at $T_1^*$ in $CsV_3Sb_5$ agrees with the first-order nature of the charge order transition[106]. Similar step-like change is also seen in single crystal samples of $RbV_3Sb_5$ (see Fig. 4e and f). It is also visible in $KV_3Sb_5$ (see Fig. 4c), but less pronounced than in its sister compounds.

In order to make sure that the observed low-temperature enhancement of the zero-field relaxation rates Γ and Δ is intrinsic and model independent, we analyzed the ZF-μSR data for $KV_3Sb_5$ considering different models beyond Eq. 3:

(1) A phenomenological model to approach an intermediate (between Gaussian and Lorentzian) fitting function by assuming only static and random distribution fields was done by Crook and Cywinsky. They modified the Kubo-Toyabe function to:

$$P_{ZF}^{GKT}(t) = \frac{1}{3} + \frac{2}{3}\left(1 - (\lambda t)^\beta\right)\exp\left[-\frac{(\lambda t)^\beta}{\beta}\right] \quad (4)$$

where, $\beta$ is in the rage of $1 < \beta < 2$. Although the parameter $\beta$ provides a continuous interpolation between purely Gaussian ($\beta = 2$) and purely Lorentzian ($\beta = 1$) static Kubo-Toyabe line-shapes, there has, as yet, been no interpretation of the physical significance of $\beta$ itself. $\lambda$ in Eq. 4 is the phenomenological muon-spin relaxation rate which relates to the width of distribution fields. This function can change the line shape smoothly between Gaussian and Lorentzian although the absolute value of $\lambda$ cannot be discussed straightforwardly in the case of a variable $\beta$. Analysis of the μSR signal taken from Up-Down detectors using Eq. 4 (power Kubo-Toyabe) alone results in a value of $\beta = 1.8$ which is lower (but close) than $\beta = 2$ expected for purely Gaussian shape. When analysing the data with the power Kubo-Toyabe multiplied by an additional exponential term then $\beta$ acquires a value of $\beta = 2$ in the whole temperature range and we obtain the same temperature dependence of both the Gaussian and exponential relaxation rates (see Fig. 4c) as the one obtained from our initial approach: Gaussian Kubo Toyabe multiplied by exponential term (see Fig. 4b). This is consistent with our original analysis showing a

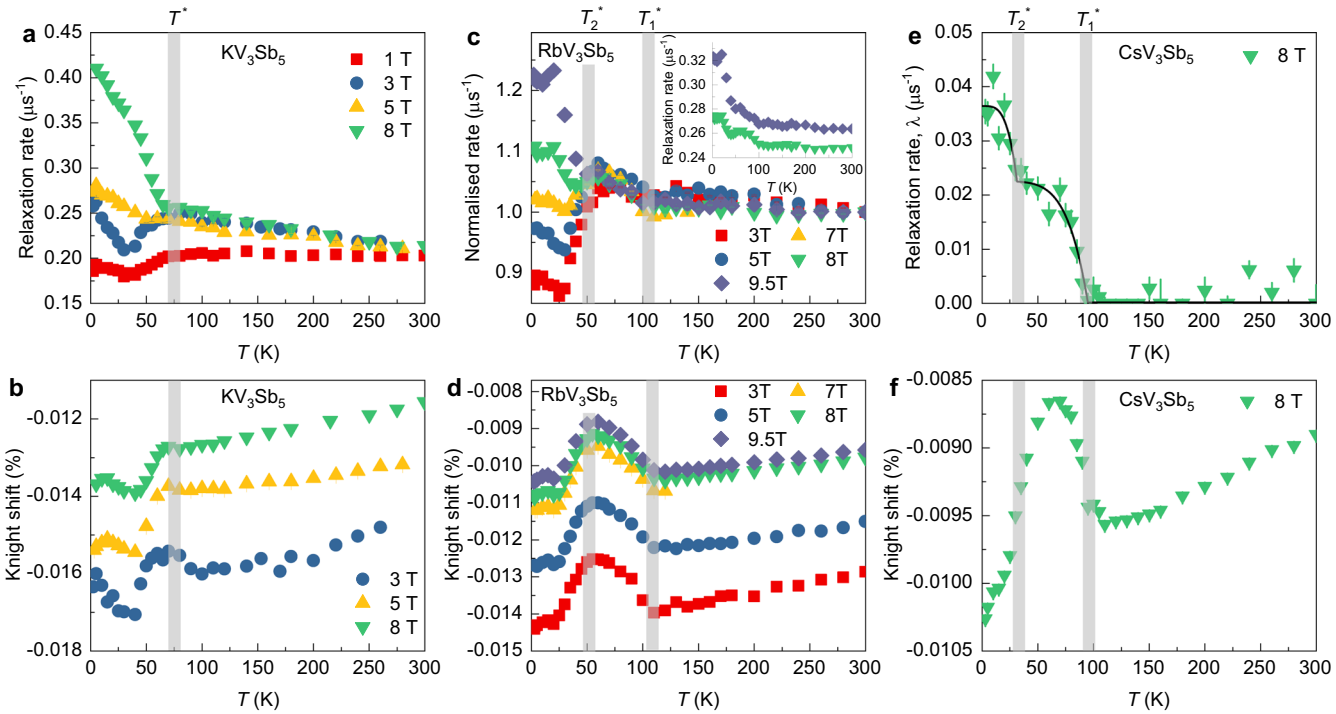


**Fig. 5 Enhanced magnetic response of the charge order in $AV_3Sb_5$ ($A$ = K, Rb, Cs) with applied external magnetic fields.** The temperature dependence of the muon spin relaxation rate (**a**, **c**, **e**) and the Knight shift $K_{exp}$ (local susceptibility) (**b**, **d**, **f**) for $KV_3Sb_5$ (**a**, **b**), $RbV_3Sb_5$ (**c**, **d**) and $CsV_3Sb_5$ (**e**, **f**), measured under the $c$-axis magnetic fields of $\mu_0H = 1$ T, 3 T, 5 T, 7 T, 8 T, and 9.5 T. The vertical gray lines mark the charge ordering temperature. The error bars represent the standard deviation of the fit parameters. The data are taken from refs. [66–68].

clear exponential relaxation for $AV_3Sb_5$. For the μSR signal taken from Forward-Backward detectors we obtained $\beta = 1.3$ which indicates a mostly Lorentzian shape of the signal (see Fig. 4c). This is consistent with the fact that the exponential relaxation rate is stronger (see $\Gamma_{12}$ in Fig. 3c) for Forward-Backward than for Up-Down detectors.

(2) We also employed the following function with the convolution of Gaussian and Lorentzian field distributions:

$$P_{ZF}^{GKT}(t) = \frac{1}{3} + \frac{2}{3}\left(1 - at - \frac{\Delta^2 t^2}{2}\right)\exp\left[-at - \frac{\Delta^2 t^2}{2}\right] \quad (5)$$

where Δ and $a$ are the width of the Gaussian and Lorentzian distribution, respectively. Eq. 5 alone does not fully describe the ZF-μSR signal. A multiplication with an additional exponential relaxation is needed. The temperature dependences of Δ, $a$ and Γ are shown in Fig. 4d. The Gaussian relaxation rate shows a similar temperature dependence as obtained from GKT * exp(-Γ$t$) model. The Lorentzian width clearly shows an increase below $T^*$. Moreover, the additional exponential rate appears only below $T^*$. In sum, both the increase of the exponential relaxation rate below $T^*$ and non-monotoneous temperature evolution of the Gaussian rate of the ZF-μSR signal for $KV_3Sb_5$ are found in all the considered models and it is independent of the analysis method.

While the ZF-μSR results, presented above, are consistent with the presence of time-reversal symmetry-breaking in charge ordered state in $AV_3Sb_5$, high-field μSR experiments are essential to confirm this effect. The onset of charge order might also alter the electric field gradient experienced by the nuclei and correspondingly the magnetic dipolar coupling of the muon to the nuclei. This can induce a change in the nuclear dipole contribution to the zero-field μSR signal. In a high magnetic field, the direction of the applied field defines the quantization axis for the nuclear moments, so that the effect of the charge order on the electric field gradient at the nuclear sites is irrelevant. The results of the high-field μSR experiments for all three samples $AV_3Sb_5$ ($A$ = K, Rb, Cs) are summarized in Fig. 5.

A non-monotonous behavior of the relaxation rate is clearly seen in the μSR data, measured in a $c$-axis magnetic field of 1 T and 3 T for $KV_3Sb_5$ and $RbV_3Sb_5$, respectively, as shown in Fig. 5a and c. The data at 1 T looks similar to the temperature dependence of the zero-field nuclear rate $\Delta_{12}$, it seems to be dominated by the nuclear response. However, at higher fields such as 3 T, 5 T, 7 T, 8 T and 9.5 T, the rate shows a clear and stronger increase towards low temperatures within the charge ordered state, similar to the behavior observed for the relaxation rates $\Gamma_{12}$ and $\Gamma_{34}$ in zero-field. Remarkably, we find that the absolute increase of the relaxation rate between the onset of charge order $T^*$ and the base-T in 8 T is 0.15 $\mu s^{-1}$ for $KV_3Sb_5$ which is a factor of six higher than the one 0.025 $\mu s^{-1}$ observed in zero-field. This shows a strong field-induced enhancement of the electronic response. As the nuclear contribution to the relaxation cannot be enhanced by an external field, this indicates that the low-temperature relaxation rate in high fields is dominated by the electronic contribution. For $RbV_3Sb_5$, the relaxation rate extracted from the high-field μSR data shows a qualitatively similar two-step increase as the ZF data at the same characteristic temperatures $T_1^* \simeq 110$ K and $T_2^* \simeq 50$ K—although the features are more pronounced at high fields (see the inset of Fig. 5c). Such a two-step increase of the relaxation rate is also observed in $CsV_3Sb_5$ (see Fig. 5e), measured under the magnetic field of 8 T, applied parallel to the $c$-axis. This indicates that the relaxation rate is strongly affected by the applied field. There is a factor of 1.5–2 enhancement of Γ below $T_2^* \simeq 30$ K and full recovery of Γ in the temperature range between $T_2^* \simeq 30$ K and $T_1^* \simeq 95$ K. It is important to note that we detect a two-step enhancement of the width of the internal magnetic field distribution sensed by the muon ensemble in $RbV_3Sb_5$ and $CsV_3Sb_5$. However, two-step transition is not well pronounced in high-field relaxation data of

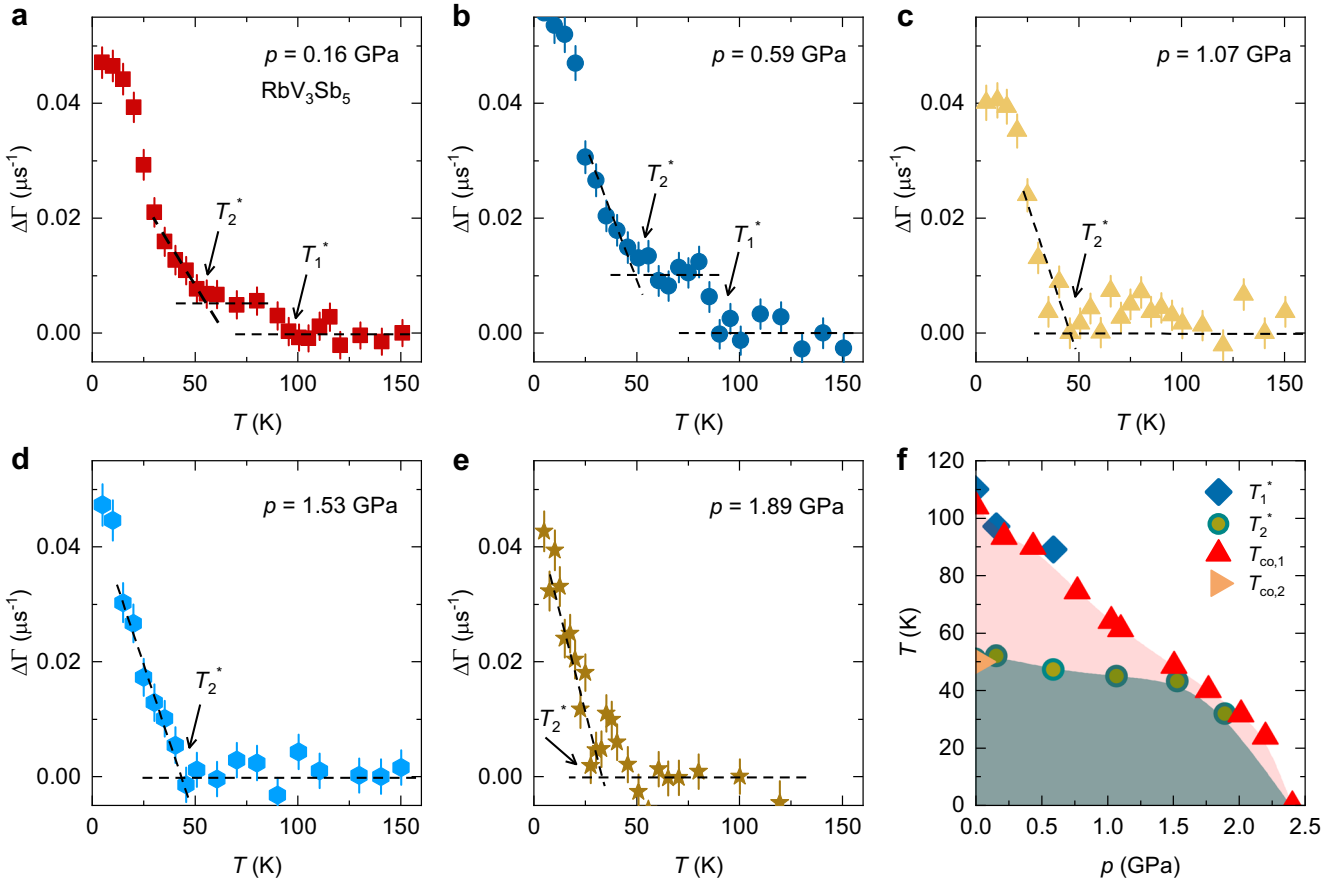


**Fig. 6 Pressure evolution of time-reversal symmetry-breaking charge orders in $RbV_3Sb_5$. a–e** The temperature dependence of the absolute change of the electronic relaxation rate $\Delta\Gamma = \Gamma(T) - \Gamma(T > 150\,\mathrm{K})$ for the polycrystalline sample of $RbV_3Sb_5$, measured at various pressures. **f** The charge order temperatures $T_{co,1}$, $T_{co,2}$ (after refs. [46,107,130]), and the onset temperatures of the time-reversal symmetry-breaking $T_1^*$, $T_2^*$ as a function of pressure. The data are taken from ref. [67].

$KV_3Sb_5$. It may be that the transitions are close to each other in high-fields and this makes it difficult to resolve two-step transition.

Figure 5b, d and f show the the temperature dependence of the experimental Knight shift (local magnetic susceptibility), measured at various applied magnetic fields, for $KV_3Sb_5$, $RbV_3Sb_5$ and $CsV_3Sb_5$, respectively. The experimental Knight shift is defined as $K_{exp} = (B_{int} - B_{ext})/B_{ext}$, where $B_{int}$ and $B_{ext}$ are the internal and externally applied magnetic fields, respectively. $K_{exp}$ shows a sharp changes across $T_1^*$ and $T_2^*$, which indicates the change of local magnetic susceptibility with two characteristic temperatures. At present, it is difficult to give a quantitative explanation on the precise origin of the temperature dependence of $K_{exp}$, but it indicates the presence of the magnetic response in all three systems concurrent with the charge order. Note however, that for a solid interpretation of the Knight shift data the signal has to be corrected for demagnetization effects which has not been done presently.

To summarize, the powerful combination of ZF-μSR and high-field μSR results show the enhanced internal field width in the charge ordered state, giving direct evidence for the time-reversal symmetry breaking fields in the kagome lattice of $AV_3Sb_5$ ($A$ = K, Rb, Cs). It is important to note that the increase of the relaxation rate arises from nearly the entire sample volume, indicating the bulk nature of the transitions below $T^*$. The current results indicate that the magnetic and charge channels of $AV_3Sb_5$ appear to be strongly intertwined, which can give rise to complex and collective phenomena.

Next, we show in Fig. 6 the evolution of the two time-reversal symmetry-breaking transition temperatures $T_1^*$ and $T_2^*$ for $RbV_3Sb_5$ with the application of hydrostatic pressure. Two step time-reversal symmetry-breaking transition is clearly observed under the pressures of $p = 0.16$ GPa and 0.59 GPa (see Fig. 6a, b). At 1 GPa, these two transitions become indistinguishable and above 1 GPa we see only transition at $T_2^*$, which decreases upon further increasing the pressure (see Figs. 6c–e). Figure 6f shows the pressure evolution of $T_1^*$ and $T_2^*$, extracted from μSR results, and of previously reported charge order temperature $T_{co,1}$[107]. The value of $T_{co,2}$[46] at ambient pressure is also shown. This phase diagram shows that two distinct time-reversal symmetry-breaking phases turn into a single time-reversal symmetry-breaking state at ~1.5 GPa, above which $T_2^*$ shows a faster suppression and follows the phase line of the charge order. Thus, this phase diagram suggests three distinct pressure regions: (a) Pressure range between 0 GPa and 1.5 GPa in which two charge order transitions are observed. (b) Pressure range between 1.5 GPa and ~2.4 GPa in which only one TRSB charge order transition is observed. (c) Pressures above ~2.4 GPa[107] where charge order is fully suppressed. Interestingly, $p_{max\text{-}Tc} = 1.5$ GPa is the pressure at which the superconducting transition temperature $T_c$ reaches its maximum value. Also, the fact that the pressure dependence of the time-reversal symmetry-breaking temperature matches well with the pressure evolution of the charge order temperature confirms the charge order being closely connected with the time-reversal symmetry-breaking in $RbV_3Sb_5$.

Finally, we would like to note that it is the collective efforts of several measurement techniques that allows us to draw the conclusion of time-reversal symmetry breaking nature of the charge order. These phenomena include the giant anomalous Hall

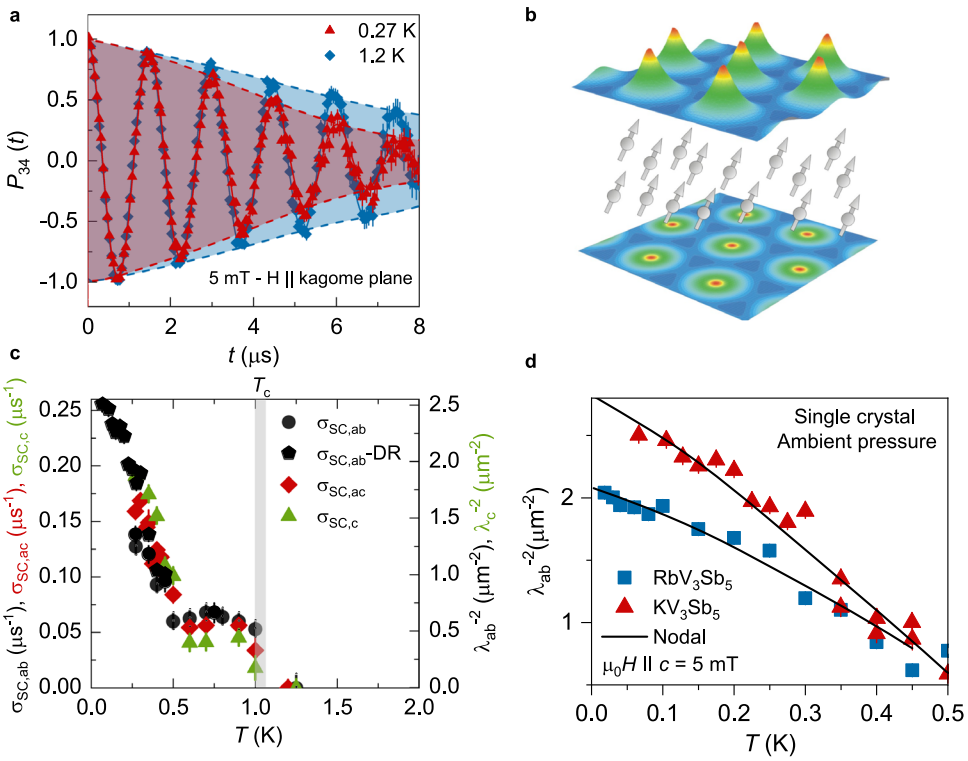


**Fig. 7 The superfluid density of $KV_3Sb_5$ and $RbV_3Sb_5$. a** The transverse field μSR spectra are obtained above and below $T_c$ (after field cooling the sample from above $T_c$). Error bars are the standard error of the mean (s.e.m.) of about $10^6$ events. The error of each bin count n is given by the standard deviation (s.d.) of n. The errors of each bin in $A(t)$ are then calculated by s.e. propagation. **b** Inset illustrates how muons, as local probes, sense the inhomogeneous field distribution in the vortex state of type-II superconductor. **c** The superconducting muon depolarization rates $\sigma_{SC,ab}$, $\sigma_{SC,ac}$, $\sigma_{SC,c}$ as well as the inverse squared magnetic penetration depth $\lambda_{ab}^{-2}$ and $\lambda_c^{-2}$ as a function of temperature, measured in 5 mT, applied parallel and perpendicular to the kagome plane. The vertical gray bar marks the superconducting transition temperature $T_c$. **d** The low-temperature part of $\lambda_{ab}^{-2}$. The solid line corresponds to a fit using a model for nodal gap superconductivity. The data are taken from ref. [67].

effect by transport[38,39], field tunable chirality switch effect[40–42], switchable chiral transport[48] and the combination of zero-field and high-field μSR experiments[66–68]. Out of these, μSR is arguably the most magnetically sensitive technique. As mentioned above, we draw the conclusion of a nuclear and an additional electronic contribution to the relaxation mainly from the high field data where the electronic contribution is very clear and spin relaxation is strongly enhanced compared to the zero field case. Theoretical modeling[50–53,55–57] of the charge ordering in the kagome lattice at van Hove filling and with extended Coulomb interactions (that is close to the condition of the $AV_3Sb_5$) also suggested that time-reversal symmetry-broken charge order with orbital currents is energetically favorable). Theoretical works[108] also suggest an enhanced orbital currents with applied magnetic field. However, the evidence for the corresponding local magnetic moments had been missing. Our μSR experiments, for the first time, provide this evidence, thus enforcing the confidence in the actual realization of the astonishing phenomenon of time reversal symmetry breaking charge order.

## Unconventional superconductivity and its interplay with charge order

The time-reversal symmetry-breaking charge order can arise from extended Coulomb interactions of the kagome lattice with van Hove singularities, where the same interactions and instabilities can lead to correlated superconductivity. Thus, we next focus on the low transverse-field μSR measurements performed in the superconducting state.

One fundamental property of the superconducting state that can directly be measured with μSR is the superfluid density. This is accomplished by extracting the second moment of the field distribution in the vortex state, which is related to the superconducting magnetic penetration depth $\lambda$ as $\langle \Delta B^2 \rangle \propto \sigma_{SC}^2 \propto \lambda^{-4}$($\sigma_{SC}$ is the superconducting muon spin depolarization rate)[66]. Because $\lambda^{-2}$ is proportional to the superfluid density, so is $\sigma_{SC}$. In order to obtain well ordered vortex lattice, the measurements should be done after field cooling the sample from above $T_c$. As an example, the TF-μSR spectra for $KV_3Sb_5$ above (1.25 K) and below (0.25 K) the superconducting transition temperature $T_c$ are shown in Fig. 7a. Above $T_c$, the oscillations show a damping essentially due to the random local fields from the nuclear magnetic moments and small contributions from the time reversal symmetry breaking charge order. The damping rate is shown to be nearly constant between 10 K and 1.25 K. Below $T_c$, the damping rate increases with decreasing temperature due to the presence of a non-uniform local magnetic field distribution as a result of the formation of a flux-line lattice (see Fig. 7b) in the superconducting state. The temperature dependences of the superconducting relaxation rates $\sigma_{SC,ab}$, $\sigma_{SC,ac}$ and $\sigma_{SC,c}$, determined (details are given in refs. [66,109]) by combining the data with the field applied along the $c$-axis and within the kagome plane, are shown in Fig. 7c. The value of the in-plane penetration depth $\lambda_{ab}$ at 0.3 K, determined from $\sigma_{SC,ab}$ (superconducting screening currents flowing parallel to the kagome plane), is found to be $\lambda_{ab} \simeq 877(20)$ nm. The value of the out-of-plane penetration depth, determined from $\sigma_{SC,c}$ (superconducting screening currents flowing perpendicular to the kagome plane), is found to be $\lambda_c \simeq 730(20)$ nm. The $\lambda(T)$ in the applied field of 5 mT shows a well pronounced two step behavior, which is reminiscent of the behavior observed in well-known two-band superconductors with a single $T_c$ such as $FeSe_{0.94}$[109] and $V_3Si$[110]. According to our numerical analysis[66] our observation of two step behavior of $\lambda(T)$ in $KV_3Sb_5$ is consistent with two gap

superconductivity with very weak interband coupling and strong electron-phonon coupling. The multi gap superconductivity is also observed for $RbV_3Sb_5$ $CsV_3Sb_5$ by means of μSR[67,69] and STM[111]. The multi-gap superconductivity in $AV_3Sb_5$ is consistent with the presence of multiple Fermi surfaces revealed by electronic structure calculations and tunneling measurements[42].

It is worthwhile noticing that the step feature in the temperature dependence of the penetration depth which we observed for $KV_3Sb_5$ is similar to the sudden decrease of the square root of the second moment of the field distribution at the vortex melting temperature in the cuprate high temperature superconductor $Bi_{2.15}Sr_{1.85}CaCu_2O_{8+\Delta}$ (BSCCO)[112]. This process is thermally activated and caused by increased vortex mobility via a loosening of the inter- or intraplanar FLL correlations. This raises the question whether the two-step transition is related to the vortex lattice melting in $KV_3Sb_5$ and $RbV_3Sb_5$. We note several arguments against such a scenario: (1) In BSCCO, the step feature occurs not in low fields (10 mT, 20 mT) but only in higher fields at which vortex lattice melting takes place[112]. In low fields the effects of the thermal fluctuations of the vortex positions on the μSR linewidth are becoming negligible and smooth temperature dependence of the linewidth is observed all the way up to $T_c$[112]. In the case of $KV_3Sb_5$ the step like feature is very well pronounced in 5 mT. With the application of 10 mT, the two-step transition becomes somewhat smoothed out and less pronounced. This is in contrast to what we expect within the scenario of vortex lattice melting. (2) The effect of the vortex lattice melting on the μSR lineshape is to change its skewness from positive (ideal static lattice) to a negative value. Thus, vortex lattice melting is clearly reflected in the line shapes. In the case of (K,Rb)$V_3Sb_5$, the SC relaxation rate (μSR linewidth) is small due to the long penetration depth and the μSR line is described by symmetric Gaussian line. Thus, it is difficult to check for the vortex lattice melting based on the shape of the field distribution. However, we carried out such an analysis for the sister compound $CsV_3Sb_5$[69] which exhibits higher superconducting critical temperature as well as a larger width of the μSR line than the $KV_3Sb_5$ sample. This allows to describe the lineshape more precisely. By analyzing the asymmetric lineshape of the field distribution and skewness parameter as a function of temperature we showed that the FLL in $CsV_3Sb_5$ is well arranged in the superconducting state and it gets slightly distorted only in the vicinity of $T_c$. But, no indication of vortex lattice melting was found in $CsV_3Sb_5$[69]. (3) We also note that the superconductors $AV_3Sb_5$ are characterized by a small superconducting anisotropy. Anisotropy of in-plane and out-of-plane penetration depth for $CsV_3Sb_5$ is only 2–3, which is two orders of magnitude smaller than the one for BSCCO. It is rather close to the values reported for Fe-based high temperature superconductors, where no vortex-lattice melting transition is observed. Considering the above arguments, we think that the two step temperature dependence of the low field magnetic penetration depth in (K,Rb)$V_3Sb_5$ is indeed due to multi-gap superconductivity with extremely small interband coupling[110]. Smearing out the step like feature with increasing the magnetic field[66,67] may be understood by the tendency of the magnetic field to suppress of one SC gap or by enhancing the interband coupling with higher fields.

In order to probe the superconducting pairing symmetry, quantitative analysis of the temperature dependence of the penetration depth $\lambda(T)$ were carried out for all three compounds as a function of pressure[66,67,69,70]. Quite generally, upon decreasing the temperature towards zero, a power-law dependence of $\lambda^{-2}(T)$ is indicative of the presence of nodal quasiparticles, whereas an exponential saturation-like behavior is a signature of a fully gapped spectrum. The low-$T$ behavior of $\lambda_{ab}^{-2}(T)$ for the single crystals of $RbV_3Sb_5$ and $KV_3Sb_5$, measured down to 18 mK and shown in Fig. 7d, displays a linear-in-$T$ behavior, consistent with the presence of gap nodes, and a small superfluid density.

To proceed with the quantitative analysis, $\lambda(T)$ was calculated within the local (London) approximation ($\lambda \gg \xi$, where $\xi$ is the coherence length) by the following expression[113]:

$$\frac{\lambda^{-2}(T,\Delta_{0,i})}{\lambda^{-2}(0,\Delta_{0,i})} = 1 + \frac{1}{\pi}\int_0^{2\pi}\int_{\Delta(T,\varphi)}^{\infty}\left(\frac{\partial f}{\partial E}\right)\frac{EdEd\varphi}{\sqrt{E^2-\Delta_i(T,\varphi)^2}}, \quad (6)$$

where $f = [1+\exp(E/k_BT)]^{-1}$ is the Fermi function, $\varphi$ is the angle along the Fermi surface, and $\Delta_i(T,\varphi) = \Delta_{0,i}\Gamma(T/T_c)g(\varphi)$ ($\Delta_{0,i}$ is the maximum gap value at $T=0$). The temperature dependence of the gap is approximated by the expression $\Gamma(T/T_c) = \tanh\{1.82[1.018(T_c/T-1)]^{0.51}\}$, while $g(\varphi)$ describes the angular dependence of the gap and it is replaced by 1 for both an $s$-wave and an $s+s$-wave gap, $|\cos(2\varphi)|$ for a $d$-wave gap, and $|\cos(3\varphi)|$ for a $f$-wave gap. To analyze the temperature dependence of the penetration depth $\lambda(T)$, we employ the empirical $\alpha$-model. The latter, widely used in previous investigations of the penetration depth of multi-band superconductors[94,114], assumes that the gaps occuring in different bands, besides a common $T_c$, are independent of each other. Then, the superfluid density is calculated for each component separately and added together with a weighting factor. For our purposes, a two-band model suffices, yielding:

$$\frac{\lambda^{-2}(T)}{\lambda^{-2}(0)} = \omega_1\frac{\lambda^{-2}(T,\Delta_{0,1})}{\lambda^{-2}(0,\Delta_{0,1})} + \omega_2\frac{\lambda^{-2}(T,\Delta_{0,2})}{\lambda^{-2}(0,\Delta_{0,2})}, \quad (7)$$

where $\lambda(0)$ is the penetration depth at zero temperature, $\Delta_{0,i}$ is the value of the $i$-th SC gap ($i=1, 2$) at $T=0$ K, and $\omega_i$ is the weighting factor which measures their relative contributions to $\lambda^{-2}$ (i.e., $\omega_1+\omega_2=1$). The $\lambda(T)$ data can also be analyzed within the framework of quasi-classical Eilenberger weak-coupling formalism, where the temperature dependence of the gaps was obtained by solving self-consistent coupled gap equations[115,116] rather than using the phenomenological $\alpha$-model, where the latter considers a similar BCS-type temperature dependence for both gaps.

The date for both $KV_3Sb_5$ and $RbV_3Sb_5$ are well described by a two-gap model, where one of the gaps has nodes and the other does not. Remarkably, we find that in both $KV_3Sb_5$ (see Fig. 8a) and $RbV_3Sb_5$ (see Fig. 8b) hydrostatic pressure induces a change from a nodal superconducting gap structure at low pressure to a nodeless, superconducting gap structure at high pressure. The crossover from nodal to nodeless pairing is correlated with the establishment of the optimal superconducting region of the phase diagram, which occurs in coincidence with a full suppression of charge order in $KV_3Sb_5$ and partial suppression of charge order in $RbV_3Sb_5$. Since the pressure at which the $T_c$ reaches the optimal value ($p_{max\text{-}Tc}$) is close to the critical pressure ($p_{co,cr}$) for the suppression of charge order, especially for the K compound, these results show that charge order strongly influences the superconducting gap structure in (Rb,K)$V_3Sb_5$, inducing nodes in an otherwise fully gapped pairing state[67]. To the best of our knowledge this is the first direct experimental demonstration of a plausible pressure-induced change in the superconducting gap structure from nodal to nodeless in these kagome superconductors. Different from $RbV_3Sb_5$ and $KV_3Sb_5$, the μSR data for $CsV_3Sb_5$ is well described by a two-gap model with both nodeles gaps which is robust under hydrostatic pressure (see Fig. 8c). Also, $CsV_3Sb_5$ shows a double peak feature both for $T_c$ and the superfluid density, leading to three distinct regions of the phase diagram.

It was also found that upon applying pressure the charge-order transitions are suppressed, and the superfluid density as well as the superconducting transition temperature increases. More specifically, the pressure values $p_{max\text{-}Tc}$ for which $T_c$ is maximum are close to the critical pressures $p_{cr,co}$ beyond which charge order is completely suppressed. In fact, as displayed in 8a, $p_{cr,co}$ essentially coincides with $p_{max\text{-}Tc}$ for $KV_3Sb_5$. Since both superconductivity and charge order occurs in the entire sample volume, there is no volume wise competition of these orders in real space.

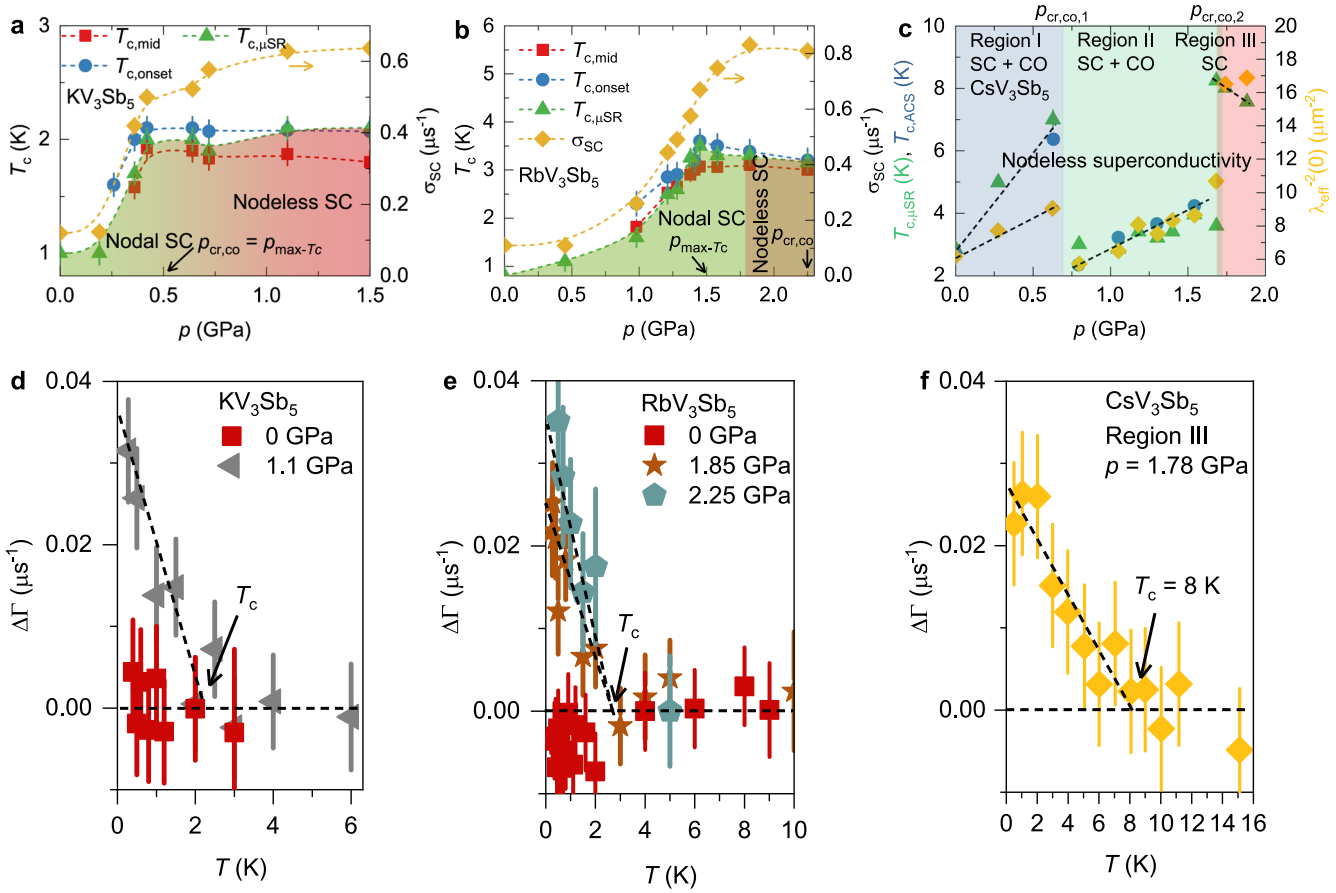


**Fig. 8 Temperature-pressure phase diagram and time-reversal symmetry-breaking superconducting state of $AV_3Sb_5$ ($A$ = K, Rb, Cs).** Pressure dependence of the superconducting transition temperature (left axis) and of the base-$T$ value of $\sigma_{sc}$ (right axis) for the samples of $KV_3Sb_5$ (**a**), $RbV_3Sb_5$ (**b**) and $CsV_3Sb_5$ (**c**). Here, $T_{c,ons}$ and $T_{c,mid}$ were obtained from AC measurements and $T_{c,\mu SR}$, from μSR. The arrows in (**a**) and (**b**) mark the critical pressure $p_{cr,co}$ at which the charge order is suppressed and the pressure $p_{max\text{-}Tc}$ at which $T_c$ reaches its maximum value. Temperature dependence of the absolute change of the electronic relaxation rate $\Delta\Gamma = \Gamma(T) - \Gamma(T > T_c)$ for $KV_3Sb_5$ (**d**), $RbV_3Sb_5$ (**e**) and $CsV_3Sb_5$ (**f**) in the temperature range across $T_c$, measured at ambient pressure and above the critical pressure at which $T_c$ is maximum. The error bars represent the standard deviation of the fit parameters. The data are taken from refs. [67,69].

They rather compete for the same electronic states in reciprocal space. In this case, competition with charge order could naturally account for the suppression of the superfluid density towards the low-pressure region of the phase diagram, where $T_{co}$ is the largest. Since charge order partially gaps the Fermi surface, as recently seen by quantum oscillation[117] and ARPES[43,118] studies, the electronic states available for the superconducting state are suppressed, thus decreasing the superfluid density[119,120].

We employed ZF-μSR analysis to probe whether there is time-reversal symmetry-breaking inside the superconducting state. Because charge order already breaks time-reversal symmetry at $T_{co} \gg T_c$, it is necessary to suppress $T_{co}$, which can be accomplished with pressure. Pressure of 1.85 GPa allows to enter the optimal $T_c$ region of the phase diagram (see Fig. 8b) in $RbV_3Sb_5$. The maximum pressure we could apply (2.25 GPa) is enough to completely suppress the charge-order in $RbV_3Sb_5$. The pressure values of $p > 0.5$ GPa and $p > 1.7$ GPa are large enough to assess the pure superconducting state of the compounds $KV_3Sb_5$ and $CsV_3Sb_5$, respectively (see Fig. 8a and c). Figure 8d, e, f show the behavior of the internal field width Γ, extracted from the ZF-μSR data, across the superconducting transition of $KV_3Sb_5$, $RbV_3Sb_5$ and $CsV_3Sb_5$, respectively, measured both at ambient pressure (red, where charge-order is present) and under applied pressures (where charge-order is absent). While at ambient pressure Γ is little affected by superconductivity, at the higher pressure there is a significant enhancement of Γ in all three systems, comparable to what has been observed in superconductors that are believed to spontaneously break time-reversal symmetry, such as $SrRu_2O_4$[102]. This provides strong evidence for time-reversal symmetry-breaking superconducting states in $AV_3Sb_5$ ($A$ = K, Rb, Cs), once optimal superconductivity is achieved, after either full or partial suppression of charge order. This is indicative of an unconventional pairing state in these systems. It is interesting to note that, to the best of our knowledge, $CsV_3Sb_5$ is the superconductor with the highest superconducting TRSB transition temperature of ≃ 8 K.

In sum, these results provide direct and so far the most convincing evidence for unconventional superconductivity in $(Rb,K,Cs)V_3Sb_5$, by combining the observations of nodal superconducting pairing and a small superfluid density at ambient pressure, which in turn displays an unconventional dependence on the superconducting critical temperature. Moreover, we find that in $(Rb,K)V_3Sb_5$ the hydrostatic pressure induces a change from a nodal superconducting gap structure at low pressure to a nodeless, time-reversal symmetry-breaking superconducting gap structure at high pressure.

## NODELESS KAGOME SUPERCONDUCTIVITY IN $LARU_3SI_2$

Besides the series of compounds $AV_3Sb_5$, presented above, the layered system $LaRu_3Si_2$[71–75] appears to be a good example of a material hosting both a kagome lattice and superconductivity. At ambient conditions, it exhibits a $T_c \simeq 7$ K[73], which is the highest

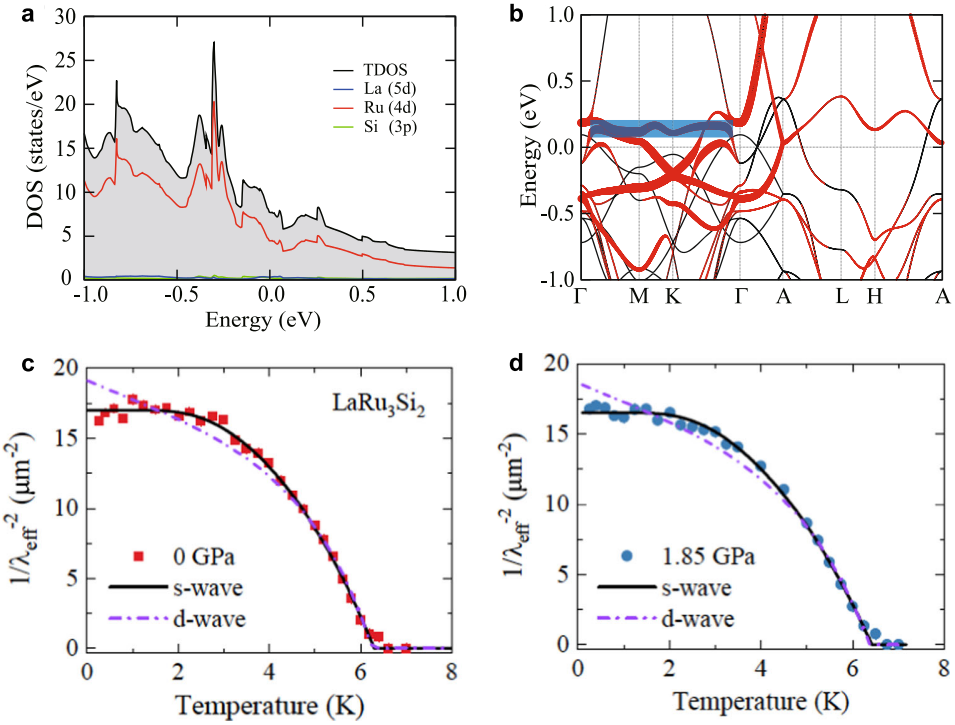


**Fig. 9 Band structure and the superfluid density in $LaRu_3Si_2$. a** The calculated total DOS and projected DOS for the Ru, Si, and La atoms in bulk $LaRu_3Si_2$. **b** The band structures (black) and orbital-projected band structure (red) for the Ru-$dz^2$ orbital without SOC along the high symmetry $k$-path. The width of the line indicates the weight of each component. The blue-colored region highlights the manifestation of the kagome flat band. The temperature dependence of $\lambda_{eff}^{-2}$ for $LaRu_3Si_2$ measured at ambient pressure (**c**) and at the maximum applied hydrostatic pressure of $p = 1.85$ GPa (**d**). The solid line corresponds to a $s$-wave model and the dashed line represents fitting with a $d$-wave model. The data are taken from ref. [76].

among the known kagome-lattice superconductors. Anomalous properties[75] in the normal and SC states[73] were reported for $LaRu_3Si_2$, such as a deviation of the normal state specific heat from the Debye model, a non-mean field like suppression of superconductivity with magnetic field and a non-linear field dependence of the induced quasiparticle density of states (DOS).

Recently, μSR experiments and first-principles calculations[76] were carried out to elucidate the superconductivity in $LaRu_3Si_2$. The calculated total and projected density of state (DOS) (Fig. 9a) demonstrate that the states at the Fermi level in $LaRu_3Si_2$ are mainly composed of Ru 4$d$ electrons. Most importantly, in the $k_z = 0$ plane, a flat band of the kagome lattice formed by the Ru-$dz^2$ orbitals is found 0.1 eV above the Fermi level, highlighted by blue-colored region in Fig. 9b. In addition, a Dirac point at the K (K′)-point with the characteristic linear dispersion is found 0.2 eV below the Fermi level. Moreover, the van Hove point on the kagome lattice at the M point can be clearly seen in Fig. 9b, which is located even closer to the Fermi energy (~50 meV). Thus, the system $LaRu_3Si_2$ exhibits, around the Fermi level, a typical kagome lattice band structure, revealing a Dirac point, the van Hove point and a dispersionless, flat band that originates from the kinetic frustration associated with the geometry of the kagome lattice. Based on the phonon dispersion, we have calculated the electron-phonon coupling constant $\lambda_{e,ph}$ to be $\simeq 0.45$[76], indicating only a moderate coupling strength in $LaRu_3Si_2$. For such a low value of $\lambda_{e,ph}$ the McMillan equation gives a precise estimate of the electron-phonon interaction induced critical temperature as discussed in ref. [121,122]. We find that electron-phonon coupling alone can only reproduce a small fraction of $T_c$, which suggests that other factors enhance $T_c$ in $LaRu_3Si_2$ such as the correlation effect from the kagome flat band, the van Hove point on the kagome lattice, and the high density of states from narrow kagome bands. However, as the flat band is 100 meV while the van Hove point is 50 meV above the Fermi energy $E_F$ it is expected that the latter has a stronger effect in the enhancement of $T_c$. This van Hove point at M is of a similar distance to $E_F$ (below $E_F$) in $KV_3Sb_5$, where it is essential to drive the $2 \times 2$ CDW order[40] at much higher temperatures than $T_c$. Moreover, we find that the whole kagome bands are relatively narrow (~300 meV), which may also enhance $T_c$ through the overall higher density of states. The narrowness of the kagome bands is similar to a group of narrow bands found in twisted bilayer graphene[123].

Zero-field (ZF)-μSR experiments just above and below $T_c$ shows no sign of either static or fluctuating magnetism down to 0.25 K[76], pointing to the absence of time-reversal symmetry-breaking superconductivity in the polycrystalline samples of $LaRu_3Si_2$. Focusing on the SC properties, the temperature dependence of $\lambda_{eff}^{-2}$ for $LaRu_3Si_2$, measured at ambient pressure (Fig. 9c) and at the maximum applied hydrostatic pressure (Fig. 9d), is best described by a momentum independent $s$-wave model with a gap value of $\Delta \simeq 1.2(1)$ meV[76]. The observed single gap superconductivity in this multi-band system implies that the superconducting pairing involves predominately one band. The measured SC gap value yields a BCS ratio $2\Delta/k_BT_c \simeq 4.3$, suggesting that the superconductor $LaRu_3Si_2$ is in the moderate coupling limit. We also note that both $\lambda_{eff}^{-2}$ and $T_c$ stay nearly unchanged under pressure, indicating a robust superconducting state of $LaRu_3Si_2$. The system $LaRu_3Si_2$ does not exhibit a CDW ground state unlike the superconductors $(K,Rb,Cs)V_3Sb_5$[40]. The fact that the $T_c$ is considerably higher than in the kagome superconductors discussed above indicates that in this case the superconductivity is not in direct competition with the charge order. However, in DFT, the stability of the crystal structure is only obtained by the addition of a Hubbard $U$[76] which suggests the proximity of this superconductor $LaRu_3Si_2$ to a CDW as $U$ usually opposes the CDW formation. Thus, the robustness of both $T_c$ and the superfluid density $\lambda_{eff}^{-2}$ of $LaRu_3Si_2$

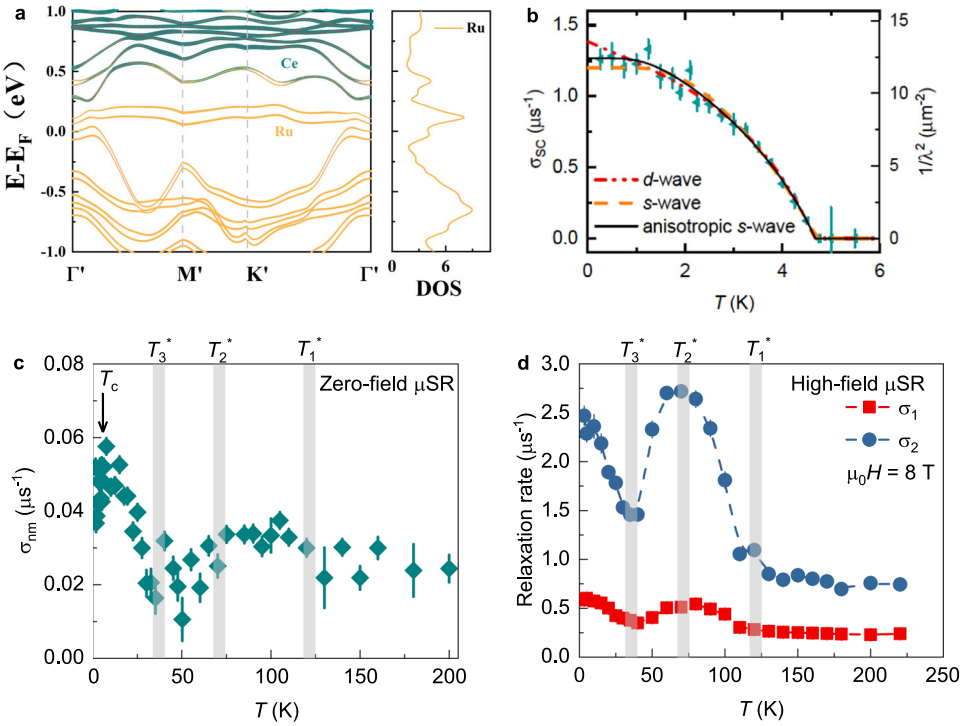


**Fig. 10 Superconducting and normal state response of $CeRu_2$.** **a** Band structure with SOC and corresponding partial density of states (PDOS). **b** Temperature dependence of the muon spin depolarization rate $\sigma_{sc}(T)$ as well as the inverse squared magnetic penetration depth $\lambda^{-2}$, measured in an applied magnetic field of $\mu_0 H = 30$ mT. The solid line corresponds to an anisotropic *s*-wave model, the dashed line corresponds to an *s*-wave model and the dotted line represents fitting with a *d*-wave model. **c** Temperature dependence of the muon spin Gaussian depolarization rate $\sigma_{nm}$, measured in zero field. The arrow marks the $T_c$ value. **d** The temperature dependences of the Gaussian muon spin relaxation rates $\sigma_1$ and $\sigma_2$, measured under a *c*-axis magnetic field of 8 T. Vertical gray bars mark the three characteristic temperatures $T_1^*$, $T_2^*$ and $T_3^*$. The data are taken from ref. [82].

to hydrostatic pressure strongly suggests that $T_c$ has the optimal value already at ambient pressure and that the system is not to close proximity to the competing CDW ground state.

Our experiments and calculations taken together point to nodeless moderate coupling time-reversal invariant kagome superconductivity in $LaRu_3Si_2$. ZF-μSR measurements of the normal state properties of $LaRu_3Si_2$ has not been carried out yet and thus we can not comment whether weak magnetic response, discovered in $AV_3Sb_5$, is also present in $LaRu_3Si_2$.

## MAGNETIC NODELESS KAGOME SUPERCONDUCTIVITY IN $CERU_2$

Another interesting superconductor with a kagome lattice is $CeRu_2$. Bulk local spectroscopic studies of the superconducting gap symmetry and the normal state properties in the single crystal of $CeRu_2$ have been carried out using a combination of zero-field (ZF)-μSR and high-field μSR experiments. From the measurements of the temperature-dependent magnetic penetration depth $\lambda$ (Fig. 10b), the superconducting order parameter exhibits an anisotropic *s*-wave gap symmetry, meaning that there is an angular dependence to the superconducting gap value (similar to *d*-wave superconductivity) but the minimum gap value is nonzero. For the ratio of the minimum gap value to the maximum gap value we obtain $\Delta_{min}/\Delta_{max} = 0.47(1)$. This is in fairly good agreement with the values $\Delta_{min}/\Delta_{max} = 0.33$ and $\Delta_{min}/\Delta_{max} = 0.20$ obtained from NMR studies[80] and in excellent agreement with the value obtained by photoemission experiments $\Delta_{min}/\Delta_{max} = 0.447$[81].

To probe the normal state response, ZF-μSR measurements over a broad temperature range were carried out. In Fig. 10c the determined zero-field relaxation rate $\sigma_{nm}$ is shown. An upturn and a broad downturn of $\sigma_{nm}$ with the onsets of $T_1^* \sim 110$ K and $T_2^* \sim 65$ K are observed. Consistent with the earlier report[124], we[82] also notice a small increase of 0.03 $\mu s^{-1}$ around 40 K, which we have denoted as $T_3^*$ in the figure. It is interesting to note the reduction of zero-field rate $\sigma_{nm}$ below the superconducting transition temperature $T_c$ (see Fig. 10c). This indicates a clear effect of superconductivity on the weak internal fields and supports the magnetic origin of the increased depolarization rate. More importantly, this behavior indicates an interplay between magnetism and superconductivity in $CeRu_2$ involving a competition for the same electronic states. Most importantly, the observed anomalies are strongly enhanced under applied magnetic field. Namely, the relaxation rate $\sigma_2$ increases by 1.5 and 1 $\mu s^{-1}$ below $T_1^*$ and $T_3^*$, respectively, in 8 T. This is two orders of magnitude higher than the increase of 0.03 $\mu s^{-1}$ observed in zero-field. This clearly supports the electronic/magnetic origin of the anomalies seen under zero-field, as the temperature dependence of the nuclear contribution to the relaxation cannot be significantly changed by an external field. The precise origin of magnetism in $CeRu_2$ is not understood. However, since macroscopic susceptibility does not show a clear magnetic transitions[82], magnetism is likely itinerant and antiferromagnetic. This calls for additional detailed experiments.

The presence of weak magnetism in $CeRu_2$ is reminiscent of the kagome superconductors $KV_3Sb_5$[66], $RbV_3Sb_5$[67] and $CsV_3Sb_5$[68,125], where μSR shows the emergence of a time-reversal symmetry-breaking state below 75 K, 110 K, and 90 K, respectively. However, in the $AV_3Sb_5$ kagome superconductors, the weak magnetic signal occurs contemporaneously with the topological charge ordering, which competes with superconductivity[67], ocurring at much lower temperatures $T_c \simeq 1$–3 K. The $T_c$ of $(K,Rb)V_3Sb_5$ are enhanced to $\simeq 4$ K under pressure, only after suppressing the charge order. Furthermore, the superconducting pairing symmetry is nodal for

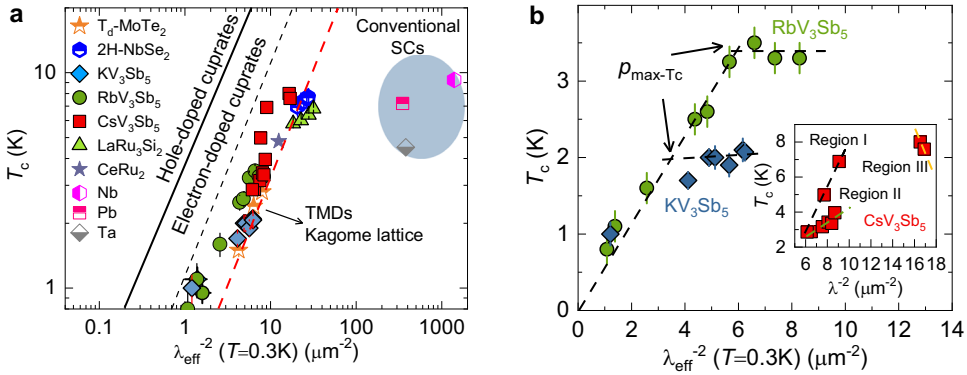


**Fig. 11 Hallmark feature of unconventional superconductivity. a** Plot of $T_c$ versus $\lambda_{eff}^{-2}(0)$ on a logarithmic scale obtained from μSR experiments for the kagome-lattice superconductors $KV_3Sb_5$[66,67], $RbV_3Sb_5$[67], $CsV_3Sb_5$[69], $LaRu_3Si_2$[76] and $CeRu_2$[82]. The dashed red line represents the relationship obtained for the layered transition metal dichalcogenide superconductors $T_d$-$MoTe_2$ and 2H-$NbSe_2$ by Guguchia et al.[8,114]. The relationship observed for cuprates is also shown[126,129] as well as the points for various conventional superconductors. **b** Plot of $T_c$ versus $\lambda_{eff}^{-2}(0)$ for $KV_3Sb_5$ and $RbV_3Sb_5$ on a linear scale. Inset shows the plot for $CsV_3Sb_5$.

both (K,Rb)$V_3Sb_5$ at low pressure when the system also exhibits charge order[67]. Upon applying pressure, the charge order is suppressed and the superconducting state progressively evolves from nodal to nodeless[67]. Thus, the high-pressure SC state in (K,Rb)$V_3Sb_5$ without charge order is nodeless. No charge ordering has been reported for $CeRu_2$ even at ambient pressure and it exhibits a nodeless superconducting state with a relatively high critical temperature $T_c \simeq 5$ K, similar to kagome superconductor $LaRu_3Si_2$. All these observations strongly suggest that the presence of charge order in kagome superconductors can strongly influence the superconducting gap structure.

## SUPERFLUID DENSITY VS THE SUPERCONDUCTING CRITICAL TEMPERATURE

To place the systems $AV_3Sb_5$, $LaRu_3Si_2$ and $CeRu_2$ in the context of other superconductors, in Fig. 11a we plot the critical temperature $T_c$ against the superfluid density $\lambda_{eff}^{-2}$ ($\lambda_{eff}$ is an effective penetration depth) on a logarithmic scale. Unconventional superconductors are characterized by a dilute superfluid (low density of Cooper pairs) while conventional BCS superconductors exhibit a dense superfluid. In other words, most unconventional superconductors have $T_c/\lambda_{eff}^{-2}$ values of about 0.1–20, whereas all of the conventional Bardeen–Cooper–Schrieffer (BCS) superconductors lie on the far right in the plot, with much smaller ratios[126–128]. Moreover, a linear relationship between $T_c$ and $\lambda_{ab}^{-2}$ is expected only on the Bose Einstein Condensate (BEC)-like side of the phase diagram[126] and is considered a hallmark feature of unconventional superconductivity, where (on-site or extended) Coulomb interactions plays a role. This relationship has in the past been used for the characterization of BCS-like, so-called conventional and BEC-like, so-called unconventional superconductors. As shown in Fig. 11a, the ratio $T_c/\lambda_{eff}^{-2}$ for unpressurized (K,Rb)$V_3Sb_5$ and $CsV_3Sb_5$ is ~0.7 K/μm$^{-2}$ and 0.45 K/μm$^{-2}$, respectively. The ratio $T_c/\lambda_{eff}^{-2}$ for $LaRu_3Si_2$ and $CeRu_2$ is nearly the same ~0.37. The value of these ratios are significantly larger compared to that of conventional BCS superconductors and lies close to either electron-doped cuprates, charge density wave superconductors $NbSe_2$[114] or Weyl-superconductor $T_d$-$MoTe_2$[8], indicative of a much smaller superfluid density. Moreover, we also find an unusual relationship between $\lambda_{eff}^{-2}$ and $T_c$ in these kagome superconductors, which is not expected for conventional superconductivity. This is presented in Fig. 11b: below $p_{max\text{-}Tc}$, the superfluid density (which is proportional to $\lambda_{eff}^{-2}$) depends linearly on $T_c$, whereas above $p_{max\text{-}Tc}$, $T_c$ barely changes for increasing $\lambda_{eff}^{-2}$. Historically, a linear increase of $T_c$ with $\lambda_{eff}^{-2}$ has been observed only in the underdoped region of the phase diagram of unconventional superconductors. Deviations from linear behavior were previously found in an optimally doped cuprate[114], in some Fe-based superconductors[94], and in the charge-ordered superconductor 2H-$NbSe_2$ under pressure[114]. Therefore, in $RbV_3Sb_5$ and $KV_3Sb_5$, it is tempting to attribute this deviation to the suppression of the competing charge ordered state by the applied pressure. More broadly, these two different dependences of $T_c$ with $\lambda_{eff}^{-2}$ indicate superconducting states with different properties below and above $p_{max\text{-}Tc}$, which is substantiated by the observation of TRS breaking superconducting state at pressures above $p_{max\text{-}Tc}$. The inset of Fig. 11b shows the correlation between $T_c$ and $\lambda^{-2}$ for $CsV_3Sb_5$. The data points for Region I (low-pressure region in Fig. 8c in which charge order pattern is the superimposed tri-hexagonal Star-of-David phase) and Region II (intermediate pressure region in Fig. 8c with the staggered tri-hexagonal phase) show the distinct slopes of the linear relation. Namely, the slope in Region I is larger by factor of 3.5 than the slope obtained for the data points from Region II. These results provide the strong evidence for a distinct competition between superconductivity and charge order in $CsV_3Sb_5$ in these two regions. In region III in which charge order is fully suppressed, $\lambda^{-2}$ is nearly independent of $T_c$. This can be attributed to the absence of a competing charge ordered state in this region.

The fact that the kagome-lattice superconductors, presented in this work, exhibit strikingly similar features in the relation between the superfluid density and the critical temperature to those reported in other unconventional superconductors implies that $AV_3Sb_5$, $LaRu_3Si_2$ and $CeRu_2$ also exhibit unconventional superconducting properties. The nearly linear relationship between $T_c$ and the superfluid density was first noticed in hole-doped cuprates in 1988-89[126–128]. The linear relationship was noticed mainly in systems lying along the line for which the ratio of $T_c$ to the effective Fermi temperature $T_F$ is about $T_c/T_F \sim 0.05$, implying a reduction of $T_c$ by a factor of 4–5 from the ideal Bose Condensation temperature for a non-interacting Bose gas composed of the same number of Fermions pairing without changing their effective masses. The results on kagome-lattice superconductors and transition metal dichalcogenides (TMDs) in Fig. 11 demonstrate that a linear relation holds for these systems, but with the ratio $T_c/T_F$ being reduced by a factor of 16-20. It was also noticed[129] that electron-doped cuprates follow another line with their $T_c/T_F$ reduced by a factor of ~4 from the line of hole doped cuprates. In ref. [127], it was discussed that there seem to exist at least two factors which determine $T_c$ in unconventional superconductors: one is the superfluid density and the other is the closeness to the competing state. Three different ratios of $T_c/T_F$ seen in the three different families of superconductors might be related to the different competing states[127]. In the case of hole-doped cuprates, the competing state is characterized by

antiferromagnetic order that is frustrated by the introduction of doped holes. In the case of electron-doped cuprates, the competing state develops in antiferromagnetic network diluted by the doped carriers. In the case of present TMD systems, the competing state comes from charge density wave or structural orders. In the case of TMDs and kagome-lattice systems, the competing state is a charge density wave. In sum, the fact that the BEC-like linear relationship may exist in systems with $T_c/T_F$ reduced by a factor 4–20 from the ratio in hole doped cuprates presents a new challenge for theoretical explanations.

In summary, we review recent experimental progress on superconducting properties and magnetic fingerprints of charge order in several kagome-lattice systems, namely $AV_3Sb_5$, $LaRu_3Si_2$ and $CeRu_2$ from the local-magnetic probe point of view. Our approach is based on combining zero-field, high-pressure and high-field muon-spin rotation methods down to ultra low temperatures, which provides a sensitive way to identify the weak electronic response of charge order and unconventional aspects of superconductivity. In this review, we presented and discussed the following results:

(1) In $AV_3Sb_5$ ($A$ = K, Rb, Cs), we show that the time-reversal symmetry breaking charge order is the normal state of these compounds at ambient pressure. The magnetic response can be enhanced by external magnetic field. In the superconducting state, we find superconductivity with a nodal energy gap in $(K,Rb)_3Sb_5$ and a nodeless energy gap in $CsV_3Sb_5$ at ambient pressure as well as a reduced superfluid density, which can be attributed to the competition with the charge order. Upon applying pressure, the charge-order transition is suppressed, the superfluid density increases, and the superconducting state progressively evolves from nodal to nodeless in $KV_3Sb_5$ and $RbV_3Sb_5$. Once charge order is eliminated, we find a superconducting pairing state that is not only fully gapped, but also spontaneously breaks time-reversal symmetry in all three systems. These results point to unprecedented tunable unconventional kagome superconductivity competing with time-reversal symmetry-breaking charge order and offer unique insights into the nature of the pairing state.

(2) In $LaRu_3Si_2$, the experiments and calculations taken together point to a moderate coupling, a nodeless gap function and to unconventional kagome superconductivity.

(3) In $CeRu_2$, the superconducting order parameter exhibits an anisotropic $s$-wave gap symmetry. Furthermore, the normal state of the system is characterized by a weak magnetic responses with the three characteristic temperatures $T_1^* \simeq 110$ K, $T_2^* \simeq 65$ K, and $T_3^* \simeq 40$ K. Therefore, our experiments classify $CeRu_2$ as a nodeless magnetic kagome superconductor.

## DATA AVAILABILITY

All relevant data are available from the authors. Alternatively, the data can be accessed through the data base at the following link http://musruser.psi.ch/cgi-bin/SearchDB.cgi.

Received: 15 May 2023; Accepted: 31 July 2023;
Published online: 18 August 2023

## REFERENCES

1. Witczak-Krempa, W., Chen, G., Kim, Y. B. & Balents, L. Correlated quantum phenomena in the strong spin-orbit regime. *Annu. Rev. Condens. Matter Phys.* **5**, 57–82 (2014).
2. Keimer, B. & Moore, J. E. The physics of quantum materials. *Nat. Phys.* **13**, 1045–1055 (2017).
3. Hasan, M. Z. & Kane, C. L. Topological insulators. *Rev. Mod. Phys.* **82**, 3045–3067 (2010).
4. Wen, X. G. Colloquium: zoo of quantum-topological phases of matter. *Rev. Mod. Phys.* **89**, 041004 (2018).
5. Bradlyn, B. et al. Topological quantum chemistry. *Nature* **547**, 298–305 (2017).
6. Hasan, M. Z., Xu, S.-Y., Belopolski, I. & Huang, S.-M. Discovery of Weyl fermion semimetals and topological Fermi arc states. *Annu. Rev. Condens. Matter Phys.* **8**, 289–309 (2017).
7. Turner, A. M., & Vishwanath, A. Beyond band insulators: Topology of semimetals and interacting phases. In Topological Insulators (pp. 293–324). (Contemporary Concepts of Condensed Matter Science; Vol. 6). https://doi.org/10.1016/B978-0-444-63314-9.00011-1 (2013).
8. Guguchia, Z. et al. Signatures of the topological $s^{+-}$ superconducting order parameter in the type-II Weyl semimetal $T_d$-$MoTe_2$. *Nat. Commun.* **8**, 1082 (2017).
9. Syôzi, I. Statistics of kagome lattice. *Prog. Theor. Phys.* **6**, 306 (1951).
10. Zhou, Y., Kanoda, K. & Ng, T.-K. Quantum spin liquid states. *Rev. Mod. Phys.* **89**, 025003 (2017).
11. Guguchia, Z. et al. Tunable anomalous Hall conductivity through volume-wise magnetic competition in a topological kagome magnet. *Nat. Commun.* **11**, 559 (2020).
12. Yin, J.-X. et al. Quantum-limit Chern topological magnetism in $TbMn_6Sn_6$. *Nature* **583**, 533–536 (2020).
13. Ghimire, N. J. & Mazin, I. I. Topology and correlations on the kagome lattice. *Nat. Mater.* **19**, 137–138 (2020).
14. Ye, L. et al. Massive Dirac fermions in a ferromagnetic kagome metal. *Nature* **555**, 638–642 (2018).
15. Nakatsuji, S., Kiyohara, N. & Higo, T. Large anomalous Hall effect in a non-collinear antiferromagnet at room temperature. *Nature* **527**, 212–215 (2015).
16. Fenner, L. A., Dee, A. A. & Wills, A. S. Non-collinearity and spin frustration in the itinerant kagome ferromagnet $Fe_3Sn_2$. *J. Phys.: Condens. Matter* **21**, 452202 (2009).
17. Han, T.-H. et al. Fractionalized excitations in the spin-liquid state of a kagome-lattice antiferromagnet. *Nature* **492**, 406–410 (2012).
18. Yan, S., Huse, D. A. & White, S. R. Spin-liquid ground state of the $S$=1/2 kagome Heisenberg antiferromagnet. *Science* **332**, 1173–1176 (2011).
19. Nayak, A. K. et al. Large anomalous Hall effect driven by a nonvanishing Berry curvature in the noncolinear antiferromagnet $Mn_3Ge$. *Sci. Adv.* **2**, e1501870 (2016).
20. Liu, E. et al. Giant anomalous Hall effect in a ferromagnetic kagome-lattice semimetal. *Nat. Phys.* **14**, 1125–1131 (2018).
21. Yin, J.-X. et al. Negative flat band magnetism in a spin-orbit coupled kagome magnet. *Nat. Phys.* **15**, 443–448 (2019).
22. Denner, M.M., Neupert, T. & Guguchia, Z. Exotic quantum phases in new kagome materials. *SPG Mitteilungen* Prog. Phys. **68** (2022).
23. Wang, W.-S. et al. Competing electronic orders on kagome lattices at van Hove filling. *Phys. Rev. B* **87**, 115135 (2013).
24. Kiesel, M. L. & Thomale, R. Unconventional fermi surface instabilities in the kagome hubbard model. *Phys. Rev. Lett.* **110**, 126405 (2013).
25. Peierls, R.E. Quantum Theory of Solids. 108 (Oxford University Press, London, 1955).
26. Kohn, W. Analytic properties of bloch waves and wannier functions. *Phys. Rev.* **115**, 809 (1959).
27. Overhauser, A. W. Exchange and correlation instabilities of simple metals. *Phys. Rev.* **167**, 691 (1968).
28. Chan, S.-K. & Heine, V. Spin density wave and soft phonon mode from nesting fermi surfaces. *J. Phys. F: Met. Phys.* **3**, 795 (1973).
29. Dressel, M. Ordering phenomena in quasi-one-dimensional organic conductors. *Naturwissenschaften* **94**, 527–541 (2007).
30. Johannes, M. D., Mazin, I. I. & Howells, C. A. Fermi-surface nesting and the origin of the charge-density wave in $NbSe_2$. *Phys. Rev. B* **73**, 205102. (2006).
31. Tranquada, J. M., Sternlieb, B. J., Axe, J. D., Nakamura, Y. & Uchida, S. Evidence for stripe correlations of spins and holes in copper oxide superconductors. *Nature* **375**, 561–563 (1995).
32. Chang, J. et al. Direct observation of competition between superconductivity and charge density wave order in $YBa_2Cu_3O_{6.67}$. *Nat. Phys.* **8**, 871–876 (2012).
33. Ortiz, B. et al. $CsV_3Sb_5$: A $Z_2$ Topological kagome metal with a superconducting ground state. *Phys. Rev. Lett.* **125**, 247002 (2020).
34. Ortiz, B. et al. Superconductivity in the $Z_2$ kagome metal $KV_3Sb_5$. *Phys. Rev. Mater.* **5**, 034801 (2021).
35. Jiang, K. et al. Kagome superconductors $AV_3Sb_5$ ($A$ = K, Rb, Cs). *Natl Sci. Rev.* **10**, nwac199 (2023).
36. Neupert, T., Denner, M. M., Yin, J.-X., Thomale, R. & Hasan, M. Z. Charge order and superconductivity in kagome materials. *Nat. Phys.* **18**, 137–143 (2022).
37. Yin, Q. et al. Superconductivity and normal-state properties of kagome metal $RbV_3Sb_5$ single crystals. *Chin. Phys. Lett.* **38**, 037403 (2021).
38. Yang, S. et al. Giant, unconventional anomalous Hall effect in the metallic frustrated magnet candidate, $KV_3Sb_5$. *Sci. Adv.* **6**, 1–7s (2020).
39. Yu, F. et al. Concurrence of anomalous Hall effect and charge density wave in a superconducting topological kagome metal. *Phys. Rev. B* **104**, 041103 (2021).

40. Jiang, Y.-X. et al. Discovery of topological charge order in kagome superconductor $KV_3Sb_5$. *Nat. Mater.* **20**, 1353–1357 (2021).
41. Shumiya, N. et al. Tunable chiral charge order in kagome superconductor $RbV_3Sb_5$. *Phys. Rev. B* **104**, 035131 (2021).
42. Wang, Z. et al. Electronic nature of chiral charge order in the kagome superconductor $CsV_3Sb_5$. *Phys. Rev. B* **104**, 075148 (2021).
43. Kang, M. et al. Twofold van Hove singularity and origin of charge order in topological kagome superconductor $CsV_3Sb_5$. *Nat. Phys.* **18**, 301–308 (2022).
44. Luo, J. et al. Possible star-of-David pattern charge density wave with additional modulation in the kagome superconductor $CsV_3Sb_5$. *NPJ Quantum Mater.* **7**, 30 (2022).
45. Yin, J.-X., Lian, B. & Hasan, M. Z. Topological kagome magnets and superconductors. *Nature* **612**, 647–657 (2022).
46. Wenzel, M. et al. Optical investigations of $RbV_3Sb_5$: Multiple density-wave gaps and phonon anomalies. *Phys. Rev. B* **105**, 245123 (2022).
47. Song, D. et al. Orbital ordering and fluctuations in a kagome superconductor $CsV_3Sb_5$. *Sci. China Phys., Mech. Astron.* **65**, 247462 (2022).
48. Guo, C. et al. Switchable chiral transport in charge-ordered kagome metal $CsV_3Sb_5$. *Nature* **611**, 461–466 (2022).
49. Hu, Y. et al. Topological surface states and flat bands in the kagome superconductor $CsV_3Sb_5$. *Sci. Bull.* **67**, 495 (2022).
50. Denner, M., Thomale, R. & Neupert, T. Analysis of charge order in the kagome metal $AV_3Sb_5$ ($A$ = K, Rb, Cs). *Phys. Rev. Lett.* **127**, 217601 (2022).
51. Christensen, M. H., Birol, T., Andersen, B. M. & Fernandes, R. M. Theory of the charge-density wave in $AV_3Sb_5$ kagome metals. *Phys. Rev. B* **104**, 214513 (2021).
52. Christensen, M. H., Birol, T., Andersen, B. M. & Fernandes, R. M. Loop currents in $AV_3Sb_5$ kagome metals: multipolar and toroidal magnetic orders. *Phys. Rev. B* **106**, 144504 (2022).
53. Ritz, E. T., Fernandes, R. M. & Birol, T. Impact of Sb degrees of freedom on the charge density wave phase diagram of the kagome metal $CsV_3Sb_5$. *Phys. Rev. B* **107**, 205131 (2023).
54. Tazai, R., Yamakawa, Y., Onari, S. & Kontani, H. Mechanism of exotic density-wave and beyond-Migdal unconventional superconductivity in kagome metal $AV_3Sb_5$ ($A$ = K, Rb, Cs). *Sci. Adv.* **8**, eabl4108 (2022).
55. Hu, Y. et al. Coexistence of Tri-Hexagonal and Star-of-David Pattern in the Charge Density Wave of the Kagome Superconductor $AV_3Sb_5$. *Phys. Rev. B* **106**, L241106 (2022).
56. Park, T., Ye, M. & Balents, L. Electronic instabilities of kagome metals: saddle points and landau theory. *Phys. Rev. B* **104**, 035142 (2021).
57. Lin, Y.-P. & Nandkishore, R. M. Complex charge density waves at van Hove singularity on hexagonal lattices: haldane-model phase diagram and potential realization in the kagome metals $AV_3Sb_5$. *Phys. Rev. B* **104**, 045122 (2021).
58. Scagnoli, V., Khalyavin, D. D. & Lovesey, S. W. Hidden magnetic order on a kagome lattice for $KV_3Sb_5$. *Phys. Rev. B* **106**, 064419 (2022).
59. Haldane, F. D. M. Model for a quantum Hall effect without Landau levels: condensed-matter realization of the parity anomaly. *Phys. Rev. Lett.* **61**, 2015–2018 (1988).
60. Varma, C. M. Non-Fermi-liquid states and pairing instability of a general model of copper oxide metals. *Phys. Rev. B* **55**, 14554–14580 (1997).
61. Nersesyan, A. A., Japaridze, G. I. & Kimeridze, I. G. Low-temperature magnetic properties of a two-dimensional spin nematic state. *J . Phys. Condens. Matter* **3**, 3353–3366 (1991).
62. Feng, X., Jiang, K., Wang, Z. & Hu, J. Chiral flux phase in the kagome superconductor $AV_3Sb_5$. *Sci. Bull.* **66**, 1384–1388 (2021).
63. Lin, Y.-P. & Nandkishore, R. Complex charge density waves at Van Hove singularity on hexagonal lattices: Haldane-model phase diagram and potential realization in kagome metals $AV_3Sb_5$. *Phys. Rev. B* **104**, 045122 (2021).
64. Wu, X. et al. Nature of unconventional pairing in the kagome superconductors $AV_3Sb_5$. *Phys. Rev. Lett.* **127**, 177001 (2021).
65. Chandan Setty, C., Hu, H., Chen, L. & Si, Q. Electron correlations and $T$-breaking density wave order in a $Z_2$ kagome metal. Preprint at https://arxiv.org/abs/2105.15204 (2021).
66. Mielke III, C. et al. Time-reversal symmetry-breaking charge order in a kagome superconductor. *Nature* **602**, 245–250 (2022).
67. Guguchia, Z. et al. Tunable unconventional kagome superconductivity in charge ordered $RbV_3Sb_5$ and $KV_3Sb_5$. *Nat. Commun.* **14**, 153 (2023).
68. Khasanov, R. et al. Time-reversal symmetry broken by charge order in $CsV_3Sb_5$. *Phys. Rev. Res.* **4**, 023244 (2022).
69. Gupta, R. et al. Microscopic evidence for anisotropic multigap superconductivity in the $CsV_3Sb_5$ kagome superconductor. *NPJ Quantum Mater.* **7**, 49 (2022).
70. Gupta, R. et al. Two types of charge order with distinct interplay with superconductivity in the kagome material $CsV_3Sb_5$. *Commun. Phys.* **5**, 232 (2022).
71. Barz, H. New ternary superconductors with silicon. *Mater. Res. Bull.* **15**, 1489–1491 (1980).
72. Vandenberg, J. M. & Barz, H. The crystal structure of a new ternary silicide in the system rare-earth-ruthenium-silicon. *Mater. Res. Bull.* **15**, 1493–1498 (1980).
73. Kishimoto, Y. et al. Magnetic susceptibility study of $LaRu_3Si_2$. *J. Phys. Soc. Jpn.* **71**, 2035–2038 (2002).
74. Li, B., Li, S. & Wen, H.-H. Chemical doping effect in the $LaRu_3Si_2$ superconductor with a kagome lattice. *Phys. Rev. B* **94**, 094523 (2016).
75. Li, S. et al. Anomalous properties in the normal and superconducting states of $LaRu_3Si_2$. *Phys. Rev. B* **84**, 214527 (2011).
76. Mielke III, C. et al. Nodeless kagome superconductivity in $LaRu_3Si_2$. *Phys. Rev. Mat.* **5**, 034803 (2021).
77. Matthias, B. T., Suhl, H. & Corenzwit, E. Ferromagnetic superconductors. *Phys. Rev. Lett.* **12**, 449 (1958).
78. Huxley, A. et al. The magnetic and crystalline structure of the Laves phase superconductor $CeRu_2$. *J. Phys. Condens. Matter* **9**, 4185–4195 (1997).
79. Deng, L. Z. et al. Magnetic kagome superconductor $CeRu_2$. Preprint at https://doi.org/10.48550/arXiv.2204.00553 (2022).
80. Kittaka, S., Sakakibara, T., Hedo, M., Onuki, Y. & Machida, K. Verification of anisotropic $s$-wave superconducting gap structure in $CeRu_2$ from low-temperature field-angle-resolved specific heat measurements. *J. Phys. Soc. Jpn.* **82**, 123706 (2013).
81. Kiss, T. et al. Photoemission spectroscopic evidence of gap anisotropy in an $f$-electron superconductor. *Phys. Rev. Lett.* **94**, 057001 (2005).
82. Mielke III, C. et al. Local spectroscopic evidence for a nodeless magnetic kagome superconductor $CeRu_2$. *J. Phys.: Condens. Matter* **24**, 485601 (2022).
83. Amato, A. Physics with muons: from atomic physics to condensed matter physics. https://www.psi.ch/en/lmu/lectures (2020).
84. Sonier, J. E., Brewer, J. H. & Kiefl, R. F. μSR studies of the vortex state in type-II superconductors. *Rev. Mod. Phys.* **72**, 769 (2000).
85. Dalmas de Reotier, P. & Yaouanc, A. Muon spin rotation and relaxation in magnetic materials. *J. Phys. Condens. Matter* **9**, 9113 (1997).
86. Amato, A. Heavy-fermion systems studied by μSR technique. *Rev. Mod. Phys.* **69**, 1119 (1997).
87. Uemura, Y. J. et al. Phase separation and suppression of critical dynamics at quantum phase transitions of MnSi and $(Sr_{1-x}Ca_x)RuO_3$. *Nat. Phys.* **3**, 29–35 (2007).
88. Blundell, S. J. Spin-polarized muons in condensed matter physics. *Contemp. Phys.* **40**, 175 (1999).
89. Guguchia, Z. Unconventional magnetism in layered transition metal dichalcogenides. *MDPI Condens. Matter* **5**, 42 (2020).
90. Schenk, A. Muon Spin Rotation Spectroscopy: Principles and Applications in Solid State. (Physics, Adam Hilger: Bristol, Engand, 1985).
91. Yaouanc, A. & Dalmas de Reotier, P. Muon Spin Rotation, Relaxation, and Resonance: Applications to Condensed Matter. (Oxford University Press, 2011).
92. Sedlak, K., Scheuermann, R., Stoykov, A. & Amato, A. GEANT4 simulation and optimisation of the high-field μSR spectrometer. *Phys. B: Condens. Matter* **404**, 970–973 (2009).
93. Khasanov, R. et al. High pressure research using muons at the Paul Scherrer Institute. *High Press. Res.* **36**, 140–166 (2016).
94. Guguchia, Z. et al. Direct evidence for a pressure-induced nodal superconducting gap in the $Ba_{0.65}Rb_{0.35}Fe_2As_2$ superconductor. *Nat. Commun.* **6**, 8863 (2015).
95. Shermadini, Z. et al. A low-background piston cylinder-type hybrid high pressure cell for muon-spin rotation/relaxation experiments. *High Press. Res.* **37**, 449–464 (2017).
96. Khasanov, R., Urquhart, R., Elender, M. & Kamenev, K. Three-wall piston-cylinder type pressure cell for muon-spin rotation/relaxation experiments. *High Press. Res.* **42**, 29–46 (2022).
97. Khasanov, R. Perspective on muon-spin rotation/relaxation under hydrostatic pressure. *J. Appl. Phys.* **132**, 190903 (2022).
98. Kenney, E. M. et al. Absence of local moments in the kagome metal $KV_3Sb_5$ as determined by muon spin spectroscopy. *J. Phys.: Condens. Matter* **33**, 235801 (2021).
99. Shan, Z. et al. Muon spin relaxation study of the layered kagome superconductor $CsV_3Sb_5$. *Phys. Rev. Res.* **4**, 033145 (2022).
100. Kubo, R. & Toyabe, T. Magnetic Resonance and Relaxation (North Holland, Amsterdam, 1967).
101. Huang, W. et al. Precision search for magnetic order in the pseudogap regime of $La_{2-x}Sr_xCuO_4$ by muon spin relaxation. *Phys. Rev. B* **85**, 104527 (2012).
102. Luke, G. M. et al. Time-reversal symmetry breaking superconductivity in $Sr_2RuO_4$. *Nature* **394**, 559 (1998).
103. Singh, A. D. et al. Time-reversal symmetry breaking and multigap superconductivity in the noncentrosymmetric superconductor $La_7Ni_3$. *Phys. Rev. B* **103**, 174502 (2021).
104. Hillier, A. D., Jorge, Q. & Cywinski, R. Evidence for time-reversal symmetry breaking in the non-centrosymmetric superconductor $LaNiC_2$. *Phys. Rev. Lett.* **102**, 117007 (2009).
105. Biswas, P. K. et al. Evidence for superconductivity with broken time-reversal symmetry in locally noncentrosymmetric SrPtAs. *Phys. Rev. B* **87**, 180503 (2013).

106. Subires, D. et al. Order-disorder charge density wave instability in the kagome metal $(Cs,Rb)V_3Sb_5$. *Nat. Commun.* **14**, 1015 (2023).
107. Wang, N. N. et al. Competition between charge-density-wave and superconductivity in the kagome metal $RbV_3Sb_5$. *Phys. Rev. Res.* **3**, 043018 (2021).
108. Tazai, R., Yamakawa, Y. & Kontani, H. Drastic magnetic-field-induced chiral current order and emergent current-bond-field interplay in kagome metal $AV_3Sb_5$ ($A = Cs,Rb,K$). Preprint at https://arxiv.org/abs/2303.00623.
109. Khasanov, R. et al. Evolution of two-gap behavior of the superconductor $FeSe_{1-x}$. *Phys. Rev. Lett.* **104**, 087004 (2010).
110. Kogan, V. G., Martin, C. & Prozorov, R. Superfluid density and specific heat within a self-consistent scheme for a two-band superconductor. *Phys. Rev. B* **80**, 014507 (2009).
111. Xu, H.-S. et al. Multiband superconductivity with sign-preserving order parameter in kagome superconductor $CsV_3Sb_5$. *Phys. Rev. Lett.* **127**, 187004 (2022).
112. Lee, S. L. et al. Evidence for two-dimensional thermal fluctuations of the vortex structure in $Bi_{2.15}Sr_{1.85}CaCu_2O_{8+\Delta}$ from muon spin rotation experiments. *Phys. Rev. Lett.* **75**, 922 (1995).
113. Brandt, E. H. Flux distribution and penetration depth measured by muon spin rotation in high-$T_c$ superconductors. *Phys. Rev. B* **37**, 2349 (1988).
114. von Rohr, F. O. et al. Unconventional scaling of the superfluid density with the critical temperature in transition metal dichalcogenides. *Sci. Adv.* **5**, eaav8465 (2019).
115. Prozorov, R. & Giannetta, R. W. Magnetic penetration depth in unconventional superconductors. *Supercond. Sci. Technol.* **19**, R41 (2006).
116. Kogan, V. G. London approach to anisotropic type-II superconductors. *Phys. Rev. B* **24**, 1572 (1981).
117. Ortiz, B. R. et al. Fermi surface mapping and the nature of charge-density-wave order in the kagome superconductor $CsV_3Sb_5$. *Phys. Rev. X* **11**, 041030 (2021).
118. Nakayama, K. et al. Multiple energy scales and anisotropic energy gap in the charge-densitywave phase of the kagome superconductor $CsV_3Sb_5$. *Phys. Rev. B* **104**, L161112 (2021).
119. Machida, K. Charge density wave and superconductivity in anisotropic materials. *J. Phys. Soc. Jpn.* **53**, 712 (1984).
120. Fernandes, R. M. & Schmalian, J. Transfer of optical spectral weight in magnetically ordered superconductors. *Phys. Rev. B* **82**, 014520 (2010).
121. McMillan, W. L. Transition temperature of strong-coupled superconductors. *Phys. Rev.* **167**, 331 (1968).
122. Carbotte, J. P. Properties of boson-exchange superconductors. *Rev. Mod. Phys.* **62**, 1027 (1990).
123. Cao, Y. et al. Correlated insulator behaviour at half-filling in magic-angle graphene superlattices. *Nature* **556**, 80 (2018).
124. Huxley, A. et al. $CeRu_2$: A magnetic superconductor with extremely small magnetic moments. *Phys. Rev. B* **54**, R9666(R) (1996).
125. Yu, L. et al. Evidence of a hidden flux phase in the topological kagome metal $CsV_3Sb_5$. Preprint at https://doi.org/10.48550/arXiv.2107.10714 (2021).
126. Uemura, Y. J. et al. Universal correlations between $T_c$ and $n_s/m^*$ (carrier density over effective mass) in High-$T_c$ cuprate superconductors. *Phys. Rev. Lett.* **62**, 2317 (1989).
127. Uemura, Y. J. et al. Condensation, excitation, pairing, and superfluid density in high-Tc superconductors: the magnetic resonance mode as a roton analogue and a possible spin-mediated pairing. *J. Phys.: Condens. Matter* **16**, S4515–S4540 (2004).
128. Uemura, Y. J. et al. Basic similarities among cuprate, bismuthate, organic, chevrel phase, and heavy-fermion superconductors shown by penetration depth measurements. *Phys. Rev. Lett.* **66**, 2665 (1991).
129. Shengelaya, A. et al. Muon-spin-rotation measurements of the penetration depth of the infinite-layer electron-doped $Sr_{0.9}La_{0.1}CuO_2$ cuprate superconductor. *Phys. Rev. Lett.* **94**, 127001 (2005).
130. Du, F. et al. Pressure-induced double superconducting domes and charge instability in the kagome metal $KV_3Sb_5$. *Phys. Rev. B* **103**, L220504 (2021).

## ACKNOWLEDGEMENTS

The μSR experiments were carried out at the Swiss Muon Source (SμS) Paul Scherrer Insitute, Villigen, Switzerland. We acknowledge the great contributions of PhD student, Charles Mielke III and the postdoctoral researchers, Dr. Debarchan Das and Dr. Ritu Gupta, to the projects. Z.G. is grateful for the productive collaboration and exchange of ideas with the group of Prof. M.Z. Hasan at Princeton University, the group of J.-X. Yin at the Southern University of Science and Technology, China, the theoretical group of Prof. T. Neupert at the University of Zürich and the theoretical groups of Prof. R.M. Fernandes and Prof. T. Birol at the University of Minnesota. We acknowledge collaboration with Prof. J. Chang at the University of Zürich, Prof. R. Thomalle at Würzburg University, Dr. M.H. Christensen at the Niels Bohr Institute, University of Copenhagen, Prof. Z.Q. Wang at Boston College, Prof. G. Xu and Dr. Y. Qin at Huazhong University of Science and Technology, Dr. E Ritz at the University of Minnesota, Prof. Q. Si at Rice University and Prof. Pengcheng Dai at Rice University. We thank group of Prof. S. Jia, Prof. Y. Shi, Prof. H. Lei and Prof. Nakatsuji for providing high quality and well characterized single crystals and polycrystalline samples. We thank Dr. R. Scheuermann for fruitful discussions. Z.G. acknowledges support from the Swiss National Science Foundation (SNSF) through SNSF Starting Grant (No. TMSGI2_211750).

## AUTHOR CONTRIBUTIONS

Z.G. was invited to contribute to the special collection "Ordered States in Kagome Metals" and he supervised the project. Figure development and writing the paper: Z.G. with contributions from H.L. and R.K. All authors discussed the results, interpretation and conclusion.

## COMPETING INTERESTS

The authors declare no competing interests.

## ADDITIONAL INFORMATION

**Correspondence** and requests for materials should be addressed to Z. Guguchia.

**Reprints and permission information** is available at http://www.nature.com/reprints

**Publisher's note** Springer Nature remains neutral with regard to jurisdictional claims in published maps and institutional affiliations.